

Individualized Gaussian process-based prediction and detection of local and global gray matter abnormalities in elderly subjects

Q1 G. Ziegler ^{a,b,*}, G. Ridgway ^a, R. Dahnke ^b, C. Gaser ^{b,c}, for The Alzheimer's Disease Neuroimaging Initiative ¹

^a Wellcome Trust Center for Neuroimaging, Institute of Neurology, London, UK

^b Department of Psychiatry, Jena University Hospital, Jena, Germany

^c Department of Neurology, Jena University Hospital, Jena, Germany

ARTICLE INFO

Article history:

Accepted 4 April 2014

Available online xxxx

Keywords:

Brain morphology

Lifespan brain aging

Gaussian processes

Single case analysis

Bayesian inference

ABSTRACT

Structural imaging based on MRI is an integral component of the clinical assessment of patients with potential dementia. We here propose an individualized Gaussian process-based inference scheme for clinical decision support in healthy and pathological aging elderly subjects using MRI. The approach aims at quantitative and transparent support for clinicians who aim to detect structural abnormalities in patients at risk of Alzheimer's disease or other types of dementia. Firstly, we introduce a generative model incorporating our knowledge about normative decline of local and global gray matter volume across the brain in elderly. By supposing smooth structural trajectories the models account for the general course of age-related structural decline as well as late-life accelerated loss. Considering healthy subjects' demography and global brain parameters as informative about normal brain aging variability affords individualized predictions in single cases. Using Gaussian process models as a normative reference, we predict new subjects' brain scans and quantify the local gray matter abnormalities in terms of Normative Probability Maps (NPM) and global z-scores. By integrating the observed expectation error and the predictive uncertainty, the local maps and global scores exploit the advantages of Bayesian inference for clinical decisions and provide a valuable extension of diagnostic information about pathological aging. We validate the approach in simulated data and real MRI data. We train the GP framework using 1238 healthy subjects with ages 18–94 years, and predict in 415 independent test subjects diagnosed as healthy controls, Mild Cognitive Impairment and Alzheimer's disease.

© 2014 Published by Elsevier Inc.

33

34

Introduction

Magnetic Resonance Imaging (MRI) and computational morphometry have become invaluable tools for in-vivo exploration of the underlying changes in healthy and pathological brain aging (Fjell and Walhovd, 2010; Friston et al., 2010). Consistent findings show that regional gray matter volume, as well as cortical thickness, exhibit substantial decline as a process of healthy aging (Fjell and Walhovd, 2010; Raz and Rodriguez, 2006). Importantly, studies observed considerable variability of age-related structural trajectories across brain regions and healthy elderly individuals (Raz et al., 2005, 2010; Walhovd et al., 2011). An open question in clinical practice still is, how to efficiently identify local pathological brain aging in individuals at risk of developing

Alzheimer's disease (AD) or other types of dementia. Due to the large individual differences of normative age-related decline, the visual assessment of healthy vs. pathological local atrophy is a challenging task even for experienced radiologists. While single case studies are long-standing practice in neuropsychology (for overview of methods see e.g. Crawford and Garthwaite, 2012; McIntosh and Brooks, 2011), there is also an increasing number of neuroimaging studies using Voxel-based Morphometry (VBM) (Ashburner and Friston, 2000; Mechelli et al., 2005) that focus on single cases in comparison to a reasonably sized group of control subjects. These studies explored voxelwise macroanatomy in patients with neurological disorders like aphasia, Huntington disease, lesions, focal cortical dysplasia, epilepsy, cortical atrophy, and dementia (Colliot et al., 2006; Maguire et al., 2010; Mehta et al., 2003; Migliaccio et al., 2012; Mühlau et al., 2009; Mummery et al., 2000; Salmond et al., 2003; Scarpazza et al., 2013; Seghier et al., 2008; Sehm et al., 2011; Woermann et al., 1999).

In order to provide statistical measures of suspicious local brain volumes (or cognitive test scores) in single case studies, several parametric techniques have been proposed. A simple approach is to calculate z-scores using the control sample mean and standard deviation. If the observed z-score is found to be less than a certain percentile of the standard normal distribution, e.g. $z < -1.645$ (corresponding to a

* Corresponding author at: Wellcome Trust Center for Neuroimaging, 12 Queen Square, WC1N 3BG London, UK.

E-mail address: g.ziegler@ucl.ac.uk (G. Ziegler).

¹ Data used in the preparation of this article were obtained from the Alzheimer's Disease Neuroimaging Initiative (ADNI) database (www.loni.ucla.edu/ADNI). As such, the investigators within the ADNI contributed to the design and implementation of ADNI and/or provided data but did not participate in analysis or writing of this report. Complete listing of ADNI investigators available at http://adni.loni.usc.edu/wp-content/uploads/how_to_apply/ADNI_Acknowledgement_List.pdf.

one-tailed 95% percentile), the deviation might be considered statistically significant. Unfortunately, the z-score approach lacks the ability to account for the uncertainty of the control sample statistics, which might inflate type I errors especially in small samples (Crawford and Howell, 1998). Thus, the more conventional parametric approach to single case inference is the two sample t-test using a ‘pooled’ estimate of the variance (for details see e.g. Mühlau et al., 2009). The t-test statistic in the special case with n controls and one single patient reduces to $t = (\mu_c - \mu_p) / (\sigma_c \sqrt{1/n + 1})$ with control sample standard deviation σ_c . Previous studies explored methodological issues using this type of unbalanced parametric design. In particular, small samples have been found to reduce sensitivity for detection of structural differences in single subjects (Mühlau et al., 2009). Unfortunately, for unbalanced designs the above difference score might be particularly affected by non-normality, rendering the t-test invalid (Salmond et al., 2002; Viviani et al., 2007). Robustness of the tests was found to be increased (type I errors reduced) by using larger smoothing kernels or appropriate transformations of the data. However, for inference in elderly subjects, the approaches often do not address the underlying developmental process, e.g. age-related effects in the control sample (see also Dukart et al., 2011), as well as variations due to other relevant covariates, e.g. global volume differences (Peelle et al., 2012).

Gaussian process (GP) models have emerged as a flexible and elegant approach for prediction of continuous, i.e. $y \in \mathbb{R}$, or binary, i.e. $y \in [0, 1]$ variables (Kim and Ghahramani, 2006; Rasmussen, 1996; Rasmussen and Williams, 2006). Recently, GPs were successfully introduced to the neuroimaging community. The potential applications range from spatial priors (Groves et al., 2009), cortical maps (Macke et al., 2011), image denoising (Zhu et al., 2012), parameter estimation (Wang et al., 2012), white matter fiber clustering (Wassermann et al., 2010) and meta-analysis (Salimi-Khorshidi et al., 2011). GP models were shown to be particularly powerful for clinical applications, providing probabilistic predictions of symptom severity, pain states, recovery, cognitive and disease states using regression (Doyle et al., 2013a; Hope et al., 2013; Marquand et al., 2010) and classification (Hahn et al., 2011; Marquand et al., 2010; Mourao-Miranda et al., 2012; Pyka et al., 2012; Young et al., 2013) using functional and structural MR images as inputs. In addition to the common application as decoding or recognition models, i.e. making inference about causes of functional and structural brain states based on images (Friston et al., 2008), GPs might be particularly useful for generative modeling of individual differences of brain morphometry (see also Ashburner and Klöppel, 2011; Friston and Ashburner, 2004).

Here we propose a new approach to support individualized clinical decisions about an elderly patient's brain structure by providing quantitative, unbiased and highly transparent maps of local gray matter abnormalities and global volume z-scores for gray matter, white matter and cerebrospinal fluid. That means, the maps and z-scores aim at information support rather than providing fixed patient-level predictions about disease states derived from ‘black-box’ classifiers. GPs are used to implement a normative generative model of elderly subjects' local and global volumes in terms of a non-parametric function of subjects' covariates. The model captures normative age-related trajectories and effects of covariates typically observed in control samples. This implicitly assumes smooth structural trajectories without imposing strong constraints on the developmental model and thus allows more flexibility than low degree polynomial expansions (for discussion of quadratic fits see e.g. Fjell et al., 2010). At the same time it accounts for region specific late life accelerated gray matter shrinkage, which is shown to be part of healthy brain aging (Fjell et al., 2012, 2013; Walhovd et al., 2011). The substantial individual differences of local and global volumes in elderly brains (i.e. even at the same age and fixed covariates) and the measurement noise are modeled in terms of Gaussian distributions and accounted for in individualized predictions. After model optimization in a large control sample, the local GP priors are conditioned on scans of new single subjects at risk of developing AD or other types of dementia.

Training with a large pooled MRI database of 1238 healthy subjects with ages 18–94 years, and testing with an independent sample from the Alzheimer's Disease Neuroimaging Initiative dataset including subjects with MCI and AD, we show that the obtained normative probability maps (NPM) and global z-scores provide a powerful clinical application by quantitatively characterizing the single patient's abnormalities as compared to age-matched neurologically normal controls. This implements a Bayesian single case inference about structural abnormalities that flexibly accounts for predictive uncertainty in practical situations of different control data sample sizes, different data noise levels, and individual patient covariates, i.e. age, brain sizes, etc.

Methods

149

A Gaussian process model of cross-sectional gray matter observations in healthy elderly

150

151

Ideally, a generative model of the normative structural aging process accurately predicts the local gray matter volume y of an elderly study participant based on the age and a set of informative covariates $\mathbf{x} = [\text{age}, \text{sex}, \dots]$, i.e. forming a low dimensional covariate space $\mathcal{D} \in \mathbb{R}^m$. The predictions require availability of most covariates for all cases in the training and test samples. Thereby, we here restrict our local generative model to six covariates summarized in $\mathbf{x}_i = [\text{age}, \text{sex}, \text{tgmv}, \text{twmv}, \text{tcsf}, \text{fstr}]$ for subject i , including demography and global parameters, i.e. total gray matter volume (tgmv), total white matter volume (twmv), and total cerebrospinal fluid (tcsf) obtained from MRI preprocessing. Furthermore, for inference about global atrophy an additional generative model for global brain parameters tgmv, twmv, and tcsf was applied using four covariates $\mathbf{x}_i = [\text{age}, \text{sex}, \text{ticy}, \text{fstr}]$ with $\text{ticy} = \text{tgmv} + \text{twmv} + \text{tcsf}$. Note, the proposed framework also naturally extends to physiological and behavioral factors, as well as subject independent but scan specific variables, e.g. the signal to noise ratio of the scan. In order to afford pooling across samples from 1.5 and 3 Tesla MRI scanners, we also included a field strength variable (fstr). The whole training sample covariate data is further denoted by \mathbf{X} , which was obtained from concatenation of rows \mathbf{x}_i for all n training subjects. The rows of brain data matrix \mathbf{Y} (with entries y_{ij}) refer to the GMV images of all n training subjects, and \mathbf{y}_j is used to denote its j -th column, i.e. the data of voxel j from all subjects. Then the lifespan generative model of gray matter in voxel j follows

$$y_{ij} = g(\mathbf{x}_i, \boldsymbol{\theta}_j) + \epsilon_{ij}, \quad \epsilon_{ij} \sim \mathcal{N}(0, \sigma_j^2) \quad (1)$$

with subject index i and hyperparameter $\boldsymbol{\theta}_j$, an additive independent identically distributed Gaussian noise (also called the likelihood model) with variance σ_j^2 . The latent (or noise free) variables $g(\mathbf{x}, \boldsymbol{\theta})$ incorporate our knowledge about aging and variability in different locations \mathbf{x} of the covariate space \mathcal{D} . We now exploit the function space perspective and define a GP prior, which implements our assumption about smoothness of the latent trajectories $g(\mathbf{x}, \boldsymbol{\theta})$. Technically, a GP is a distribution of functions, which is fully specified by its mean and its covariance function (for a technical introduction see Rasmussen and Williams, 2006)

$$g \sim \mathcal{GP}(m, cov). \quad (2)$$

188

The following specification of the prior mean m and covariance function cov implies a distribution over latent structural trajectories and their individual differences in voxel j

189

190

$$m(g(\mathbf{x}_p, \boldsymbol{\theta}_j)) = 0 \quad (3)$$

$$\text{cov}\left(g(\mathbf{x}_p, \boldsymbol{\theta}_j), g(\mathbf{x}_q, \boldsymbol{\theta}_j)\right) = k_{\boldsymbol{\theta}_j}(\mathbf{x}_p, \mathbf{x}_q). \quad (4)$$

The main idea here is to suppose the covariance of the latent local and global volumes $g(\mathbf{x}, \boldsymbol{\theta}_j)$ to be a function of the similarities among subjects in covariate space \mathcal{D} , expressed by a kernel mapping k . However, because the contribution of each dimension of \mathcal{D} to latent variables g is a-priori unknown, we implement the kernel using a squared exponential function with automatic relevance determination (ARD) (Neal, 1996) for each voxel j

$$k_{\boldsymbol{\theta}_j}(\mathbf{x}_p, \mathbf{x}_q) = a_j \exp\left(-\frac{1}{2} (\mathbf{x}_p - \mathbf{x}_q)^T \text{diag}(\boldsymbol{\gamma}_j)^{-2} (\mathbf{x}_p - \mathbf{x}_q)\right), \quad (5)$$

with covariance hyperparameter $\boldsymbol{\theta}_j = (a_j, \boldsymbol{\gamma}_j)$, i.e. amplitude a_j and characteristic length scales $\boldsymbol{\gamma}_j = [\gamma_1^{(j)}, \dots, \gamma_4^{(j)}]$ corresponding to axes of space \mathcal{D} (similarly with 4 dimensions for global models). In particular, smaller values of length scale $\boldsymbol{\gamma}^{(j)}$ indicate shorter timescales of lifespan developmental dynamics in voxels j . Intuitively, this parametrization of the kernel mapping symbolizes that either males or females with similar ages and global parameters are expected to have similar latent local gray matter volumes. Using the compact matrix notation the above model implies the following covariance for observed local gray matter volumes in voxel j

$$\text{Cov}(\mathbf{y}_j) = \mathbf{K}_{\boldsymbol{\theta}_j} + \sigma_j^2 \mathbf{I}, \quad (6)$$

with \mathbf{y}_j referring to a column vector of all observations in voxel j , $\mathbf{K}_{\boldsymbol{\theta}_j} \equiv \mathbf{K}_{\boldsymbol{\theta}_j}(\mathbf{X}, \mathbf{X})$ denoting the evaluated kernel $k_{\boldsymbol{\theta}_j}$ for all pairs of training points \mathbf{X} using the covariance hyperparameters $\boldsymbol{\theta}_j$, and σ_j^2 again denotes the noise model variance. A more compact way to introduce the above model and the Gaussian process prior in Eqs. (1)–(4) using conditionals is

$$p(\mathbf{y}_j | \mathbf{g}_j) = \mathcal{N}(\mathbf{g}_j | \sigma_j^2 \mathbf{I}) \quad (7)$$

$$p(\mathbf{g}_j | \mathbf{X}) = \mathcal{N}(0, \mathbf{K}_{\boldsymbol{\theta}_j}). \quad (8)$$

We introduce the marginal likelihood by marginalization over the latent function values \mathbf{g}_j using the likelihood $p(\mathbf{y}_j | \mathbf{g}_j, \mathbf{X})$ and the prior $p(\mathbf{g}_j | \mathbf{X})$

$$p(\mathbf{y}_j | \mathbf{X}) = \int p(\mathbf{y}_j | \mathbf{g}_j, \mathbf{X}) p(\mathbf{g}_j | \mathbf{X}) d\mathbf{g}_j. \quad (9)$$

The logarithm of the GP prior term can be further evaluated

$$\log p(\mathbf{g}_j | \mathbf{X}) = -\frac{1}{2} \mathbf{g}_j^T \mathbf{K}_{\boldsymbol{\theta}_j}^{-1} \mathbf{g}_j - \frac{1}{2} \log |\mathbf{K}_{\boldsymbol{\theta}_j}| - \frac{n}{2} \log 2\pi. \quad (10)$$

The integration over Gaussian likelihood and prior can be performed analytically (for details Rasmussen and Williams, 2006) and reveals the log marginal likelihood (or evidence) for the lifespan generative model of voxel j

$$\log p(\mathbf{y}_j | \mathbf{X}) = -\frac{1}{2} \mathbf{y}_j^T \left(\mathbf{K}_{\boldsymbol{\theta}_j} + \sigma_j^2 \mathbf{I} \right)^{-1} \mathbf{y}_j - \frac{1}{2} \log |\mathbf{K}_{\boldsymbol{\theta}_j} + \sigma_j^2 \mathbf{I}| - \frac{n}{2} \log 2\pi. \quad (11)$$

Model optimization for local and global models is performed using the conjugate gradient descent of the marginal likelihood, which is supposed to optimally balance data-fit (term one in Eq. (11)) and model parsimony (term two). All applications using

GP inference and prediction on MRI data in this paper were performed using Gaussian Process Regression and Classification Toolbox 3.4 (GPML, <http://www.gaussian-process.org/gpml/code/matlab/doc/in-dex.html>). 238 239 240

Normative probability maps and global z-scores

241

The above generative lifespan model of local and global volumes affords individualized predictions for untrained patients at risk of disease related abnormalities. We denote the optimized model parameters with $\hat{\boldsymbol{\theta}}_j$ and $\hat{\sigma}_j^2$. The corresponding test sample covariates and brain images are supposed to be contained in rows of matrices \mathbf{X}^* and \mathbf{Y}^* respectively. For the purpose of predictions in a clinical decision setting, we first consider the joint distribution of already observed gray matter values \mathbf{y}_j and latent variables of new test subjects \mathbf{g}_j^* , i.e.

244 245 246 247 248 249

$$\begin{bmatrix} \mathbf{y}_j \\ \mathbf{g}_j^* \end{bmatrix} \sim \mathcal{N} \left(0, \begin{bmatrix} \mathbf{K}_{\hat{\boldsymbol{\theta}}_j} + \hat{\sigma}_j^2 \mathbf{I} & \mathbf{K}_{\hat{\boldsymbol{\theta}}_j}(\mathbf{X}, \mathbf{X}^*) \\ \mathbf{K}_{\hat{\boldsymbol{\theta}}_j}(\mathbf{X}^*, \mathbf{X}) & \mathbf{K}_{\hat{\boldsymbol{\theta}}_j}(\mathbf{X}^*, \mathbf{X}^*) \end{bmatrix} \right). \quad (12)$$
251

We obtain the predictive distribution of local gray matter volume for the patient's latent variables (see also Rasmussen and Williams, 2006)

252

$$\begin{aligned} p(\mathbf{g}_j^* | \mathbf{X}, \mathbf{y}_j, \mathbf{X}^*, \hat{\boldsymbol{\theta}}_j, \hat{\sigma}_j^2) &= \mathcal{N}(\bar{\mathbf{g}}_j^*, \text{Cov}(\mathbf{g}_j^*)), \quad \text{with} \\ \bar{\mathbf{g}}_j^* &= \mathbf{K}_{\hat{\boldsymbol{\theta}}_j}(\mathbf{X}^*, \mathbf{X}) [\mathbf{K}_{\hat{\boldsymbol{\theta}}_j} + \hat{\sigma}_j^2 \mathbf{I}]^{-1} \mathbf{y}_j \\ \text{Cov}(\mathbf{g}_j^*) &= \mathbf{K}_{\hat{\boldsymbol{\theta}}_j}(\mathbf{X}^*, \mathbf{X}^*) - \mathbf{K}_{\hat{\boldsymbol{\theta}}_j}(\mathbf{X}^*, \mathbf{X}) [\mathbf{K}_{\hat{\boldsymbol{\theta}}_j} + \hat{\sigma}_j^2 \mathbf{I}]^{-1} \mathbf{K}_{\hat{\boldsymbol{\theta}}_j}(\mathbf{X}, \mathbf{X}^*). \end{aligned} \quad (13)$$
254 255 256 257

By adding the local noise variance $\hat{\sigma}_j^2$ to the latent predictive variance we arrive at the predictive distribution for observed local gray matter in the test sample, given the incorporated knowledge about healthy structural aging in the training sample

258 259 260

$$p(\mathbf{y}_j^* | \mathbf{X}, \mathbf{y}_j, \mathbf{X}^*, \hat{\boldsymbol{\theta}}_j, \hat{\sigma}_j^2) = \mathcal{N}(\bar{\mathbf{y}}_j^*, \text{Cov}(\mathbf{y}_j^*) + \hat{\sigma}_j^2 \mathbf{I}). \quad (14)$$
259 260

To implement a Bayesian single case inference, we evaluate the z-scores of the predictive distribution

260 261 262

$$\delta_{ij} = \frac{y_{ij}^* - \bar{y}_{ij}^*}{u_{ij}}, \quad (15)$$
262 263

$$u_{ij}^2 = k_{\hat{\boldsymbol{\theta}}_j}(\mathbf{x}_i^*, \mathbf{x}_i^*) - k_{\hat{\boldsymbol{\theta}}_j}(\mathbf{x}_i^*, \mathbf{X})^T \left(\mathbf{K}_{\hat{\boldsymbol{\theta}}_j} + \hat{\sigma}_j^2 \mathbf{I} \right)^{-1} k_{\hat{\boldsymbol{\theta}}_j}(\mathbf{x}_i^*, \mathbf{X}) + \hat{\sigma}_j^2. \quad (16)$$
263 264

The central ideas are illustrated in Fig. 1. The local z-scores δ_{ij} of test subject i at voxel j form the core of the proposed abnormality detection technique and will be denoted Normative Probability Maps (NPMs). The NPMs provide whole brain maps that reflect the probability to observe a particular patient's value (or even smaller values) of gray matter volume in a voxel, given the knowledge about structural lifespan development incorporated in the above generative model. The global z-scores were obtained analogous to the local NPMs. Strictly speaking, the exact probabilities would be obtained from evaluation of the cumulative predictive distribution. Nevertheless, this integration is expected to provide skewed distributions and thus might lack simplicity for practical clinical applications. Alternatively, we define the NPMs using z-scores, distributed around zero, with more negative values indicating stronger atrophy compared to normals and larger positive values showing hypertrophy respectively. The evaluation of local and global z-scores of the predictive probability densities sets the expected values for δ_{ij} for subjects drawn from the training population to zero. This additionally has the effect of normalizing the expected values across voxels. Note,

264 265 266 267 268 269 270 271 272 273 274 275 276 277 278 279 280 281 282

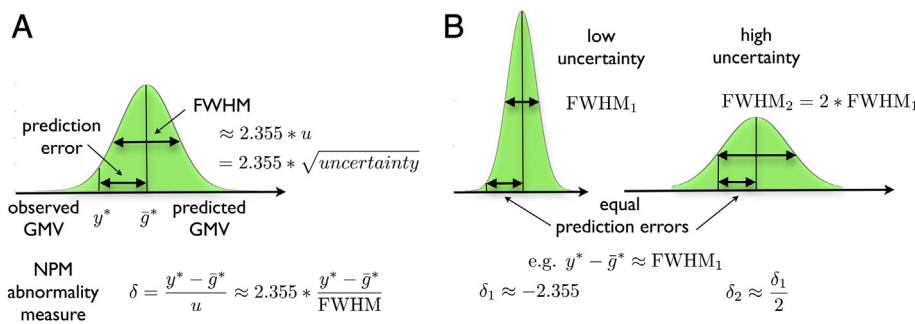


Fig. 1. Illustration of the predictive distribution and core elements of the abnormality detection method. (A) The predictive distribution $p(y^* | \mathbf{X}, \mathbf{y}, \mathbf{x}^*, \hat{\theta}, \sigma^2)$ of an arbitrary voxel given the database covariates, database gray matter volumes, the test subject covariates, the optimized hyperparameters and local noise variance is shown in green. Its mode is the predicted gray matter volume \bar{g}^* for the test subject. The difference of observed and predicted gray matter volume $y^* - \bar{g}^*$ we denote prediction error. The spread of the predictive distribution is called the predictive variance (or uncertainty) u^2 (with $FWHM \propto u$). The core of the method (and entries of NPMs) are abnormality measures δ , the z-scores, i.e. the prediction error in the unit of standard deviation of the predictive distribution. That is, δ evaluates the prediction error while accounting for differences of predictive uncertainty across subjects and voxels. (B) We illustrate that the NPMs appropriately account for uncertainty differences in all predictions. The prediction error $y^* - \bar{g}^*$ indicates the unexpected atrophy or hypertrophy under the generative model of normal aging. Then, observing the same prediction error in two subjects (or brain voxels) for instance with fourfold uncertainty (or equivalently twice FWHM) results in half of the value of δ and thus indicates less severe evidence for abnormality of the test subject.

that using NPMs for single case inference combines the prediction error, i.e. which here denotes the difference of observed and predicted volumes $y_{ij}^* - \bar{g}_{ij}^*$ (and which should not be confused with accuracy), and the predictive uncertainty u_{ij}^2 , i.e. the variance of the predictive distribution. Intuitively, the advantage of such a Bayesian modeling approach for clinical decision support is that two predictions indicating the same prediction error (in the spirit of $y_{ij}^* - \bar{g}_{ij}^*$) can also be associated with very different levels of certainty or confidence (see Fig. 1B). NPMs and global z-scores account for these confidence differences and the model's predictions will strongly affect our conclusions for low compared to high predictive uncertainty. Inspecting the terms of the uncertainty (Eq. (16)) one can observe that it is increased by the prior variance and the noise term, and reduced by the information that the training sample provides about the test case.

297 Clinical decisions based on NPMs

In contrast to common multivariate decoding schemes in dementia research (for review see Klöppel et al., 2012), our GP model affords inference about the local and global gray matter volume atrophies, which is an inference about the consequences rather than the cause, i.e. the disease status $D = [\text{healthy, AD, LewyBody, etc.}]$ (see also Friston and Ashburner, 2004). However, we aim to show that NPMs and global z-scores might support the clinical decision process by providing a likelihood model for the implicit inference performed by the clinician. A reasonable inference about underlying disease states D_i would be obtained by applying Bayes-rule

$$P(D_i | \text{scan}) = \frac{P(\text{scan} | D_i) P(D_i)}{P(\text{scan})}. \quad (17)$$

If we further make the simplifying assumption of conditional independence across voxels denoted with y_1, \dots, y_l

$$P(\text{scan} | D_i) = P(y_1, \dots, y_l | D_i) \approx P(y_1 | D_i) \dots P(y_l | D_i) \quad (18)$$

we arrive at the approximate posterior distribution for disease states

$$P(D_i | \text{scan}) \approx \frac{P(D_i)}{P(\text{scan})} \prod_{j=1}^l P(y_j | D_i). \quad (19)$$

A clinician following a naive Bayesian inference about the unknown disease state of an individual with a brain scan (and gray matter volumes y) might implicitly apply mental representation of disease priors $P(D_i)$ (obtained from clinical experience) and the likelihood under

different generative models for competing hypotheses $P(y_j | D_i)$. We therefore assume that medical expert's decision can be supported by providing quantitative, valid, and transparent likelihood maps. The above introduced z-scores provide a measure of the likelihood of observing y_j under the generative model of healthy aging, i.e. $P(y_j | D_i = \text{healthy})$, and thus might form a useful reference for all decisions about alternative disease states.

Application to simulated data

In order to demonstrate the validity and potential of the proposed GP model, we used ground truth simulations followed by an application to real MRI data. The simulations were designed to emphasize two major purposes of the model outlined in the following two sections.

Predictions of sparsely sampled individual developmental trajectories based on subject's covariates

The GP model affords accurate between-subject level predictions for gray matter observations in samples with large individual differences and age-related effects. The predictions are made using a set of subject's covariates, e.g. age, demography, or other brain parameters. In order to realize simulations we here suppose (A) that gray matter observations in healthy development and aging essentially stem from sparse temporal sampling of an ensemble \mathcal{E} of individual trajectories and (B) that the considered covariates of interest are physiological or behavioral correlates or contributors to the variability within the ensemble. We formalize these assumptions by introducing the following two-level mixed-effects model of the ensemble of trajectories \mathcal{E} . The first level model is based on the assumption that the trajectory of underlying volumetric changes is sampled from subject specific functions of age or time

$$y_{ij} = f(t_{ij}, \boldsymbol{\theta}_i^{(1)}) + \epsilon_{ij}^{(1)} \quad (20)$$

where the measurement y_{ij} is the j -th observations obtained from the i -th subject at time (age) t_{ij} , and $\epsilon_{ij}^{(1)}$ denotes a Gaussian measurement error. In particular, we parameterize the trajectory using a quadratic polynomial expansion of age $f(t_{ij}, \boldsymbol{\theta}_i^{(1)}) = \theta_{0i} + \theta_{1i}t_{ij} + \theta_{2i}t_{ij}^2$. This first level of the ensemble can be further summarized by $\mathbf{y} = X^{(1)}\boldsymbol{\theta}^{(1)} + \epsilon^{(1)}$. Although the true individual change parameters $\boldsymbol{\theta}_i^{(1)}$ might be unknown, we here suppose to have access to their physiological or behavioral correlates, i.e. subject specific effects $X_c = [x_1, \dots, x_r]$, e.g. demographic variables, or global brain parameters, etc.

354 The contribution of these covariates to the first level change param-
355 eters is described by the second level model

$$\boldsymbol{\theta}^{(1)} = \mathbf{X}^{(2)} \boldsymbol{\theta}^{(2)} + \boldsymbol{\epsilon}^{(2)} \quad (21)$$

357 with the parameters $\boldsymbol{\theta}^{(2)}$ and design matrix $\mathbf{X}^{(2)}$ containing three col-
358 umns of ones for each θ_{0i} , θ_{1i} and θ_{2i} and further columns for the covari-
359 ates X_c . Notably, Gaussian noise $\boldsymbol{\epsilon}^{(2)}$ adds further random individual
360 differences to the ensemble of trajectories. The purpose of applying a
361 nonparametric GP model in this context of mixed-effects models of de-
362 velopment, i.e. assuming $f \sim \mathcal{GP}(m, cov)$, is that it affords predictions for
363 measures of brain structure y_{ij} based on observations of individual covari-
364 ates X_c without knowing the explicit parametrization of trajectory
365 shape $f(t, \theta)$, the information about temporal sampling contained in
366 $\mathbf{X}^{(1)}$, and the structure of the ensemble in design matrix $\mathbf{X}^{(2)}$. That
367 means, GP model optimization corresponds to learning the functional
368 form of a generative process. Fig. 2A depicts 100 trajectories of the sim-
369 ultated healthy subjects ensemble with either large (left) or small (right)
370 individual differences. In order to obtain a typical cross-sectional sam-
371 ple of local gray matter volumes we assumed a single MRI scan per sub-
372 ject at random adult lifespan age (see red crosses in Fig. 2A). The
373 observations y_{1i} were then modeled as a nonparametric GP function
374 using subject's age and covariates of individual change parameters x_{0i} ,
375 x_{1i} and x_{2i} as inputs, i.e. corresponding to θ_{0i} , θ_{1i} , and θ_{2i} respectively.
376 The trained GP model allows predictions of observations in an inde-
377 pendent ensemble of healthy subjects (Fig. 2B). We further varied the
378 strength of correlation of accessible covariates and ground truth change
379 parameters $\text{corr}(x_k, \theta_k) = 0, 0.25, 0.5, 0.75$, and 1. As expected, we
found that observing covariates that exhibit stronger relationships to

380 the ground truth parameters of the mixed-effects generative process,
381 affords better predictions in the cross-sectional sample. In order to com-
382 pare the GP based predictions to existing methods, we additionally
383 computed predictions for the test ensemble using general linear
384 model (GLM) estimates in the ensemble used for training. Fig. 2C de-
385 picts mean absolute error of predictions in an independent test ensem-
386 ble based on squared exponential covariance GP and GLM. Predictive
387 performance was compared using either only subject's age or age to-
388 gether with three covariates x_{0i} , x_{1i} and x_{2i} . We independently varied
389 the total amount of individual differences in terms of the second level
390 error in the ensemble and the amount of noise in terms of the first
391 level error. The obtained simulation for nonlinear trajectories suggests
392 the advantages of GP based compared to GLM based predictions for dif-
393 ferent contexts of developmental data. 393

Inference about local gray matter volume abnormalities in pathological 394 aging trajectories 395

We further explored the potential of GP based inference about 396 gray matter abnormalities in pathological aging. Having captured 397 the large age-related variance and further individual differences in 398 a healthy sample of brain development and aging, we here aim at 399 evaluating the likelihood of unseen test subjects' brain scans given 400 the database as a normative reference. We therefore simulated an 401 ensemble of trajectories from diseased subjects \mathcal{E}_d by assuming a 402 substantial additive linear disease process beginning at a random age 403 of onset θ_{4j} : $f(t_{ij}, \theta_i^{(1)}) = \theta_{0j} + \theta_{1j}t_{ij} + \theta_{2j}t_{ij}^2 + \theta_{3j} \cdot \max([0, t_{ij} - \theta_{4j}])$. 404 With exception of this disease process, this parametrization of the tra- 405 jectories is assumed to be identical to the ensemble of healthy subjects 406

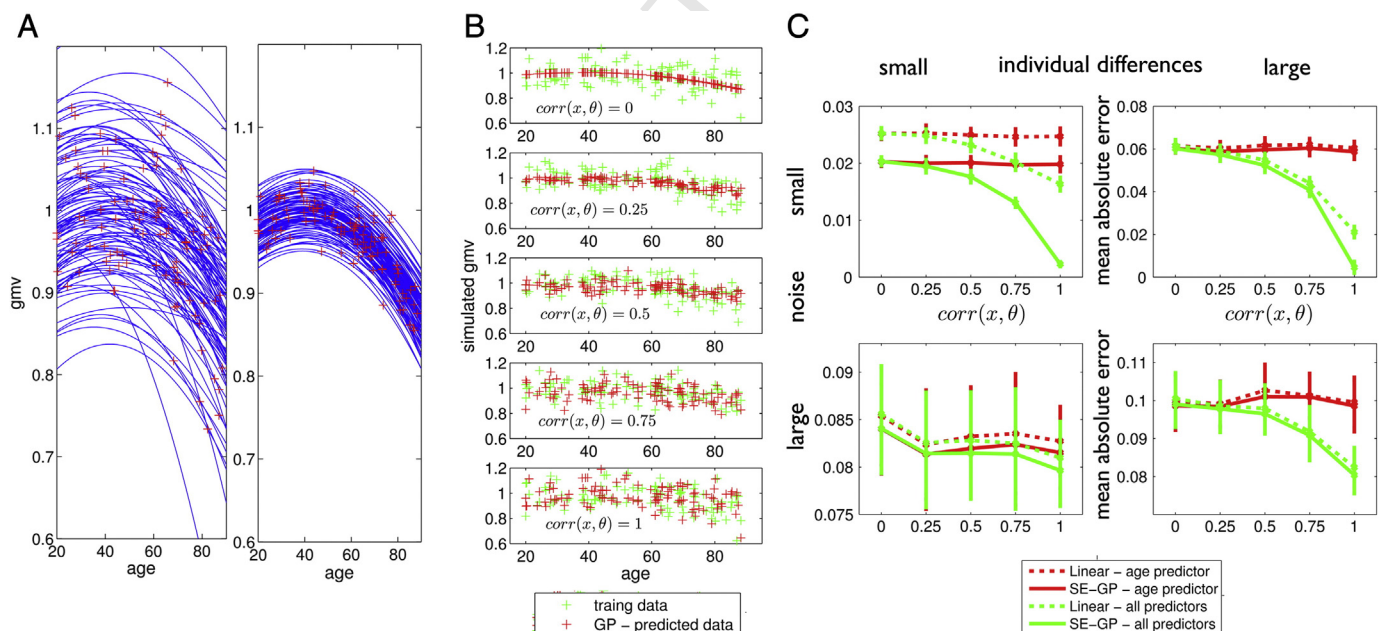


Fig. 2. Simulation of structural trajectories, cross-sectional sampling and predictions based on correlates of individual change parameters. (A) Illustration of simulation of data y_{1i} for $i = 1, \dots, 640$ subjects using the mixed-effects modeling framework described in Eqs. (20) and (21). Two random ensembles of individual trajectories using a quadratic model parametrization $f(t_{ij}, \theta_i^{(1)}) = \theta_{0i} + \theta_{1i}t_{ij} + \theta_{2i}t_{ij}^2$ with expectation of change parameters $E(\theta_i^{(1)}) = \boldsymbol{\theta}^{(2)} = [0.92, 4 \cdot 10^{-3}, 1 \cdot 10^{-4}]$ and either large individual differences (A left) with $\text{Var}(\theta_i^{(1)}) = \text{diag}([6 \cdot 10^{-3}, 1 \cdot 10^{-6}, 2 \cdot 10^{-10}])$ or small individual differences (A right) with $\text{Var}(\theta_i^{(1)}) = \text{diag}([6 \cdot 10^{-4}, 1 \cdot 10^{-7}, 2 \cdot 10^{-11}])$. Only 100 trajectories are shown. Red crosses indicate cross-sectional observations corresponding to a sparse sampling of trajectories with a single MRI observation per subject i at age t_{1i} distributed uniformly over the adult lifespan [20, 90]. Observations were performed with additive i.i.d. Gaussian noise with either $\text{Var}(\epsilon_{ij}^{(1)}) = 0.01$ (large noise) or $6 \cdot 10^{-6}$ (small noise) respectively. Independent training and test ensembles were simulated. The second level model (Eq. (21)) also included random correlates/covariates $\mathbf{x}_i = [x_{0i}, x_{1i}, x_{2i}]$ of ground truth individual change parameters θ_i under variation of the correlation size to the true change parameter, i.e. $\text{corr}(x_k, \theta_k) = 0, 0.25, 0.5, 0.75, 1$. (B) Gaussian process based predictions (using Eq. (14)) of observations y_{1i} based on subject covariates \mathbf{x}_i after training in one ensemble and testing in a second independent ensemble. Rows illustrate the increase of precision of predictions under different correlation sizes $\text{corr}(x, \theta)$. (C) Mean absolute error of predictions for small and large amounts of noise (first level error) and individual differences (second level error) for a GP model with squared exponential covariance ('SE-GP') and predicting the same data using the general linear model ('Linear') estimated in the training data. Both, predictions using only subject's age and using all individual covariates, i.e. $[age, x_{0i}, x_{1i}, x_{2i}]$, indicate improvements in using the Gaussian process model for different types of data.

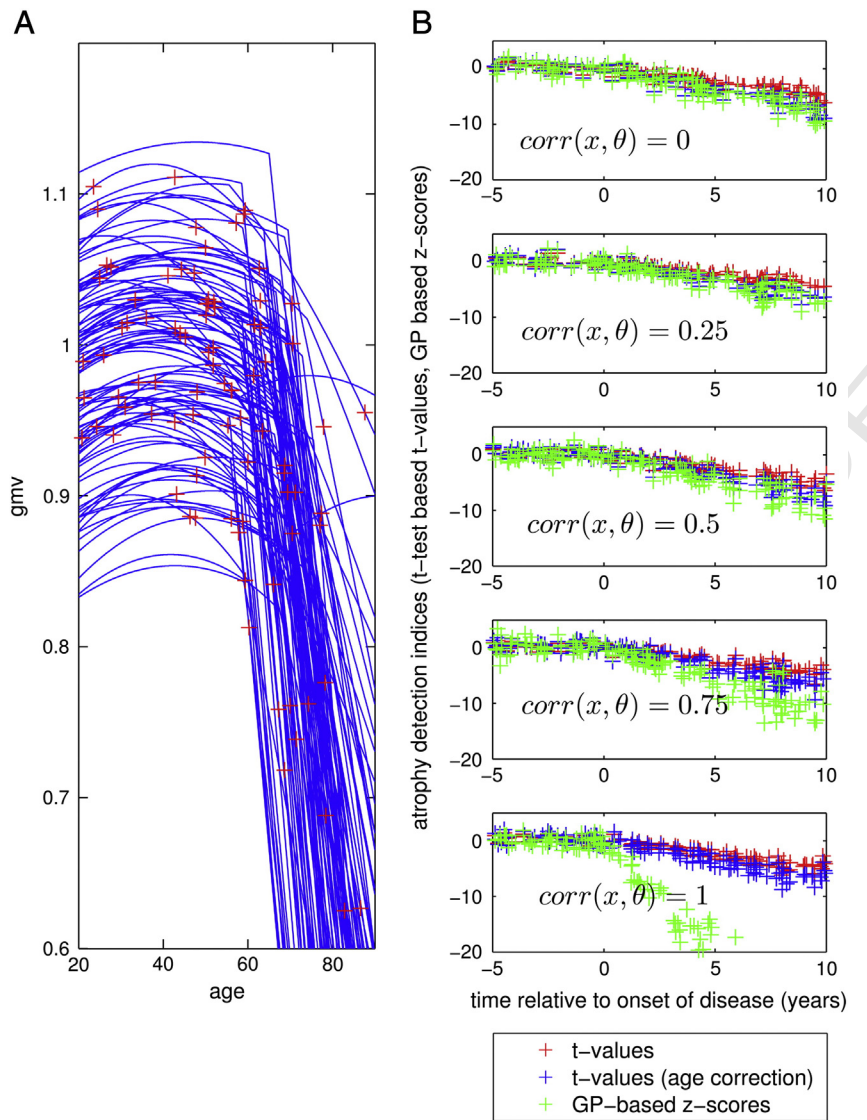


Fig. 3. Simulation of an ensemble of structural trajectories with additive disease process and comparison of methods for their detection in an ensemble of healthy trajectories. (A) Illustration of simulations of observations y_{it} for $i = 1, \dots, 640$ from diseased subjects using the mixed-effects modeling framework described in Eqs. (20) and (21). The random ensemble of individual trajectories followed the healthy subject quadratic model with additional linear decline after individual age of onset at age θ_{4i} : $f(t_{ij}, \boldsymbol{\theta}_j^{(1)}) = \theta_{0i} + \theta_{1i}t_{ij} + \theta_{2i}t_{ij}^2 + \theta_{3i} \cdot \max([0, t_{ij} - \theta_{4i}])$ with expectation of change parameters $E(\boldsymbol{\theta}^{(1)}) = \boldsymbol{\theta}^{(2)} = [0.92, 4 \cdot 10^{-3}, 1 \cdot 10^{-4}, -0.02, 65]$ and individual differences defined by $\text{Var}(\boldsymbol{\theta}_j^{(1)}) = \text{diag}([(16 \cdot 10^{-3}, 1 \cdot 10^{-6}, 2 \cdot 10^{-10}, 1 \cdot 10^{-4}, 20)])$. Only 100 trajectories are shown. Red crosses indicate cross-sectional observations similar to the healthy ensemble. Observations were performed with additive i.i.d. Gaussian noise with noise $\text{Var}(\epsilon_{ij}^{(1)}) = 2 \cdot 10^{-5}$. (B) Comparison of different statistics for detection of increased atrophy in 640 healthy and 640 diseased test subjects using single case inference based on an independent healthy control sample. T-values $t = (\mu_c - \mu_p) / (\sigma_c \sqrt{1/n + 1})$ (see Introduction) are depicted in red over individual time of onset of disease. T-test after correction for age-effects in control and test sample is shown in blue. Proposed Gaussian process based z-scores (Eq. (15)) are shown in green. GP training is performed on an independent healthy ensemble of trajectories. Rows show different correlation sizes of the covariates (used for prediction with GP) with the true change parameter.

Fig. 3A depicts 100 trajectories of simulated diseased subjects and the random age of MRI acquisition. In this context of mixed-effects models for development and aging, early disease detection corresponds to classifying new subjects based on a single observation into ensembles \mathcal{E} and \mathcal{E}_d respectively. As a proof of principle, we here compared the GP-based z-scores and t-values with respect to their ability to detect the abnormality of diseased subjects after the age of onset. Fig. 3B compares z-scores, and t-values, and t-values with correction of age effects in the control and test sample as a function of years relative to the individual onset of disease. We found that all considered indices exhibit comparable values before the age of onset. However, after disease onset the z-scores showed a steeper decline with years after onset compared to t-tests. This indicates an increased sensitivity for early disease detection, in particular using more informative covariates with higher

correlation to the ground truth individual differences of the generative process. Based on the above assumptions, this finding indicates the potential of using informed predictions to access deviations from normality in real MRI data applications.

Application to real MRI data

Database

The GP models of normative aging were trained using a large cross-sectional healthy aging brain database, which has been pooled using healthy controls' T1-weighted MRI scans from four freely available multi-center samples. Firstly, we included 116 healthy controls' (ages 60–90 years, mean age 75.9 years) baseline/screening

432 scans from the ADNI1 dataset of the Alzheimer's Disease Neuroimaging
 433 Initiative (ADNI, <http://www.adni-info.org>)² (see also Mueller
 434 et al., 2005). Secondly, 316 healthy controls (ages 18–94, mean age
 435 45.1 years) from the cross-sectional release of the Open Access Series
 436 of Imaging Studies (OASIS, <http://www.oasis-brains.org>) entered
 437 the database (Marcus et al., 2007). Thirdly, 561 subjects
 438 (19–85 years, mean age 48.0 years) from the IXI database (<http://biomedic.doc.ic.ac.uk/brain-development>) were included. Finally,
 439 245 participants (19–85 years, mean age 44.5 years) from the International
 440 Neuroimaging Data-sharing Initiative (INDI, http://fcon_1000.projects.nitrc.org/indi/indi_ack.html) Functional Connectome
 441 Project/INDI imaging sites Atlanta, Baltimore, Berlin, Cambridge,
 442 ICBM, Leiden, Milwaukee, Muenchen, and New-York entered the
 443 training sample (for additional information see Mennes et al.,
 444 2013). The sample selection of healthy elderly subjects was per-
 445 formed in order to realize a sufficient coverage of the adult lifespan
 446 age range. Apart from the chronological age, we did not apply any
 447 additional phenotypic information-based inclusion criteria. After ex-
 448 cluding subjects with artifacts or errors during the MRI preprocess-
 449 ing steps (see section below) and pooling the subsamples we
 450 obtained the final VBM database for subsequent GP model training
 451 ($n = 1238$, 686/552 female/male, ages 18–94 years, mean 49.7, std
 452 19.7). Notably, 245 subjects from the INDI sample and 180 subjects
 453 from the IXI sample were scanned with 3 Tesla scanners, while all
 454 other subjects in training and testing were scanned with 1.5 Tesla
 455 scanners. The differences due to variations of scanner field strength
 456 were explicitly accounted for in the subsequent modeling steps.
 457 The database samples densely over the adult lifespan containing
 458 288/175/164/190/169/188/64 subjects with ages 18–30, 31–40,
 459 41–50, 51–60, 61–70, 71–80, and 81–94 years respectively. Further-
 460 more, we chose a large subsample of the ADNI1 database with T1-
 461 weighted scans of 415 study participants with ages 55–93 years to
 462 detect local brain abnormalities. This independent test sample
 463 contained 100 baseline scans of healthy subjects, 95 with a stable di-
 464 agnosis of MCI during the whole ADNI study (sMCI), 92 converting
 465 from original MCI diagnosis at baseline to AD during the ADNI
 466 study (pMCI), and 128 scans of patients diagnosed with AD. Note,
 467 that we chose random non-overlapping subsamples of the ADNI
 468 healthy subjects for training and testing. This affords valid testing
 469 of the generalization capability of our approach.

472 Image preprocessing

473 A detailed overview of the acquisition protocols can be found on
 474 the corresponding project references. From the available samples
 475 we included T1-weighted images with a maximum voxel dimension
 476 of 1.5 mm. All further preprocessing steps were performed in SPM8
 477 ([Wellcome Trust Centre for Neuroimaging, London, UK, http://www.fil.ion.ucl.ac.uk/spm](http://www.fil.ion.ucl.ac.uk/spm)) using the VBM8 toolbox (<http://dbm>.

² Data used in the preparation of this article were obtained from the Alzheimer's Disease Neuroimaging Initiative (ADNI) database (adni.loni.ucla.edu). The ADNI was launched in 2003 by the National Institute on Aging (NIA), the National Institute of Biomedical Imaging and Bioengineering (NIBIB), the Food and Drug Administration (FDA), private pharmaceutical companies and non-profit organizations, as a \$60 million, 5-year public–private partnership. The primary goal of ADNI has been to test whether serial magnetic resonance imaging (MRI), positron emission tomography (PET), other biological markers, and clinical and neuropsychological assessment can be combined to measure the progression of mild cognitive impairment (MCI) and early AD. Determination of sensitive and specific markers of very early AD progression is intended to aid researchers and clinicians to develop new treatments and monitor their effectiveness, as well as lessen the time and cost of clinical trials. The Principal Investigator of this initiative is Michael W. Weiner, MD, VA Medical Center and University of California-San Francisco. ADNI is the result of efforts of many co-investigators from a broad range of academic institutions and private corporations, and subjects have been recruited from over 50 sites across the U.S. and Canada. The initial goal of ADNI was to recruit 800 adults, ages 55 to 90, to participate in the research, approximately 200 cognitively normal older individuals to be followed for 3 years, 400 people with MCI to be followed for 3 years and 200 people with early AD to be followed for 2 years. For up-to-date information, see www.adni-info.org.

neu-ro.uni-jena.e/vbm). During preprocessing all images were inter- 479 polated to an isotropic resolution of 1.5 mm. The images were (1) 480 corrected for bias-field inhomogeneities, (2) registered using a linear 481 (i.e. 12-parameter affine) and a nonlinear diffeomorphic transform- 482 ation (Ashburner, 2007), and (3) stripped of non-brain tissue in 483 the T1-weighted images. Thereafter, some results from the SPM8 484 unified segmentation package (Ashburner and Friston, 2005) were 485 used to initialize a VBM8 algorithm that classifies brain tissue into 486 gray matter (GM), white matter (WM), and cerebrospinal fluid (CSF). 487 In order to avoid introducing a systematic bias into the segmentation 488 of adult and elderly subjects' brains the applied segmentation is prior 489 free. The VBM8 segmentation contains partial volume estimation 490 (PVE) to account for mixed voxels with two tissue types (Tohka et al., 491 2004). The algorithm uses an adaptive maximum a posteriori (AMAP) 492 approach (Rajapakse et al., 1997) and a subsequent application of a hid- 493 den Markov random field model (Cuadra et al., 2005). Within the AMAP 494 estimation, the local variations of the parameters (means and variance) 495 are modeled as slowly varying spatial functions. This accounts for inten- 496 sity inhomogeneities and other local variations. We further quality 497 checked the database using covariance-based inhomogeneity measures 498 of the sample as implemented in the VBM8 toolbox. Thereafter, the 499 resulting gray matter volume images were multiplied voxelwise by 500 the determinants of Jacobian matrices from SPM's nonlinear transfor- 501 mations. This modulation is done to adjust for local volume changes in- 502 troduced by the nonlinear normalization. Finally, in order to explore the 503 effects of different degrees of smoothing we reran all GP models using 504 Gaussian kernels of 4, 8, and 12 mm full width at half maximum 505 (FWHM) respectively. The images were masked by a binary image indi- 506 cating voxelwise sample mean of gray matter volume exceeding abso- 507 lute threshold of 0.05. All GP modeling steps were performed on 508 subsamples of database images obtained using the above steps. To re- 509 duce computational expense the local GP optimization and predictive 510 map predictions were performed in a downsampled 3 mm grid obtain- 511 ed from the 7th degree B-spline interpolation. The obtained 52,252 gray 512 matter voxels from 1238 subjects were assumed to reflect aging-related 513 differences, as well as normative individual variability in terms of fine- 514 grained maps of local gray matter volume (GMV) content. 515

516 Transformation of the data

Recent work on Voxel-based Morphometry methods has explored 517 conditions, under which parametric tests may reveal invalid conclu- 518 sions (Viviani et al., 2007). In particular, the authors showed that severe 519 departures from normality of local gray matter volume distributions 520 may affect significance thresholds, especially for highly unbalanced de- 521 signs. Although classical frequentist and Bayesian inference schemes are 522 fundamentally different, similar violations of the normality assumptions 523 might introduce biases in our model estimates. As suggested by Viviani 524 et al. (2007), applying heterogeneous voxel-by-voxel transformations 525 might reduce non-normality and its consequences. We follow a similar 526 approach by entering the preprocessed data to a voxelwise Box–Cox 527 power transformation (Box and Cox, 1964) of the following form 528

$$f_{\lambda}(y) = \begin{cases} \frac{y^{\lambda}-1}{\lambda} & \text{if } \lambda \neq 0 \\ \log(y) & \text{if } \lambda = 0. \end{cases} \quad (22)$$

The local parameter λ for each voxel was chosen by maximization of 530 the log-likelihood function

$$L(\lambda) = -\frac{n}{2} \log \sigma_{\lambda}^2 + \log J_{\lambda}, \quad (23)$$

with the number of training samples n , the estimated residual vari- 533 ance σ_{λ}^2 under the maximum likelihood fit of the transformed data, 534 and the Jacobian of the transformed data J_{λ} . In order to preserve 535 the voxelwise scaling of the transformed data for further modeling

steps, we normalized the transformed data according to f_λ . Due to the nonlinearity of mapping f_λ approximate normalization can be achieved using linear Taylor expansion around the mean μ , i.e. $f_\lambda(y) \approx f_\lambda(\mu) + f'_\lambda(\mu)(y - \mu)$, from which follows that $Var(y) \approx Var(f_\lambda(y)/f'_\lambda(\mu))$. Note, the local data transformation is a separate modeling step performed before subsequent GP modeling steps. This local parameter λ was determined using only the training database and further reused to transform the testing sample images in a similar way.

544 Results

In order to demonstrate the validity of the proposed GP framework for local and global abnormality detection in neuroimaging data, we trained the above specified models using the large healthy subject database. The noise variance captures the remaining variance in the observations unexplained by variability in covariate space. Fig. 4A depicts the obtained spatial pattern of the noise from data smoothed with a Gaussian kernel of 8 mm FWHM. With the exception of the thalamus, most cortical gray matter regions exhibited reasonably small noise variance. At the same time the evidence closely resembled the spatial pattern of the noise term, with higher evidence in regions with less unexplained variance in observations (Fig. 4B, left). Increased spatial smoothness in the observations reduced the local amount of noise and increased the model evidence. At least in part, this might be related to regional variance differences of modulated local gray matter volume after between-subject normalization (Fig. 4B right plot). Histograms of whole brain voxelwise characteristic length scales are shown in Fig. 4C. The proposed model is symmetric with respect to the dimensions of the covariate space and a projection on the age dimension reveals adult lifespan local structural trajectories (Fig. 4D).

An assumption that affords computationally tractable and efficient local GP model inference is the Gaussianity of the noise model. Moreover, any violations of Gaussianity might result in biased single case

predictions and inference. As suggested by Ashburner and Friston (2000) the quantile–quantile (Q–Q) plot might provide a normality statistic for the model residuals. The Q–Q plots sample quantile versus the sample quantile that would be expected if the residuals were normally distributed. If so, a Q–Q plot would result in a straight line. A deviation from a straight line can be identified by calculating the correlation coefficient of the Q–Q plot. The expected and observed Q–Q plot correlation coefficients for our database are shown in Fig. 5A (left). The correlations were mainly observed in the interval [0.99, 1] but nevertheless exhibited slight deviations from the theoretical expectation under normality. We explored these deviations by calculating the third and fourth standardized moments of residuals, i.e. skewness and kurtosis respectively. As expected for modulated gray matter volume data, the residuals show a slightly positive skewness for many voxels (see Fig. 5A middle). Additionally, but less emphasized, kurtosis was found to be slightly higher than three indicating a more peaky distribution with heavier tails (see Fig. 5A right). Application of larger smoothing kernel sizes improved normality but left a noticeable positively skewed distribution of observations, even with large smoothing kernels. As recently suggested by Viviani et al. (2007) we explored the benefits of local Box–Cox transformation of the gray matter volume observations before subsequent GP modeling. Fig. 5B depicts Q–Q plot correlations and standardized moments of the model residuals after the transformation. Applying Box–Cox transform to the data substantially improved the Gaussianity by reducing residuals' skewness toward the expectations under normality assumptions.

Fig. 6 illustrates the single hippocampus voxel (at 24, −12, −18 MNI) local model (top row) and the three global models (bottom row) for each tissue class. In order to afford visualization, we only show the dependency on age and global parameters (top row) and on age and total intracranial volume (bottom row) using 3D surface plots. Models of local and global brain parameters indicate that GPs are able to capture nonlinear dependencies in the data. The core of GP model is the full posterior distribution of predictive latent variables,

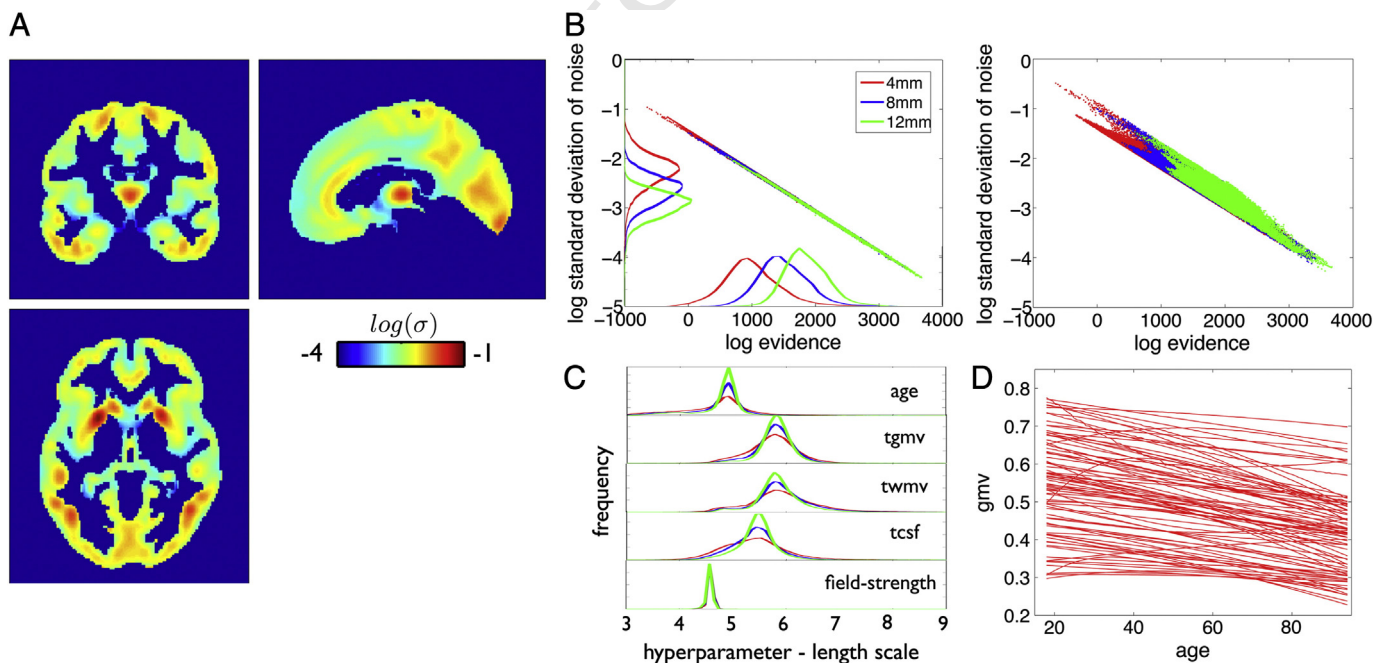


Fig. 4. Gaussian process generative model of local gray matter volume using 1238 healthy adult subjects with ages 18–94 years. (A) The estimated local noise term $\log(\hat{\sigma})$ of the GP model for data after smoothing with 8 mm Gaussian kernel is shown. The noise term captures unexplained variability of gray matter volume observations. Red and blue indicate larger vs. smaller local noise variance, respectively. (B) Shown is the relationship of local model evidence and the noise term $\log(\hat{\sigma})$ (log log plot) across all voxels for different degrees of smoothing (left). In particular, by applying Gaussian kernels of 4 (red), 8 (blue), and 12 (green) mm FWHM. Additionally histograms of the corresponding indices are shown. The relationship of local model evidence and the standard deviation of gray matter volume observations (log log plot) across all voxels is shown for different degrees of smoothing (right). (C) Histogram of voxelwise length scale parameters $l_i^{(j)}$ of the input variables obtained from model optimization. (D) 100 random voxel lifespan gray matter volume trajectories of the estimated generative model. Shown is $g(x, \theta_j)$ as a function of subject's age.

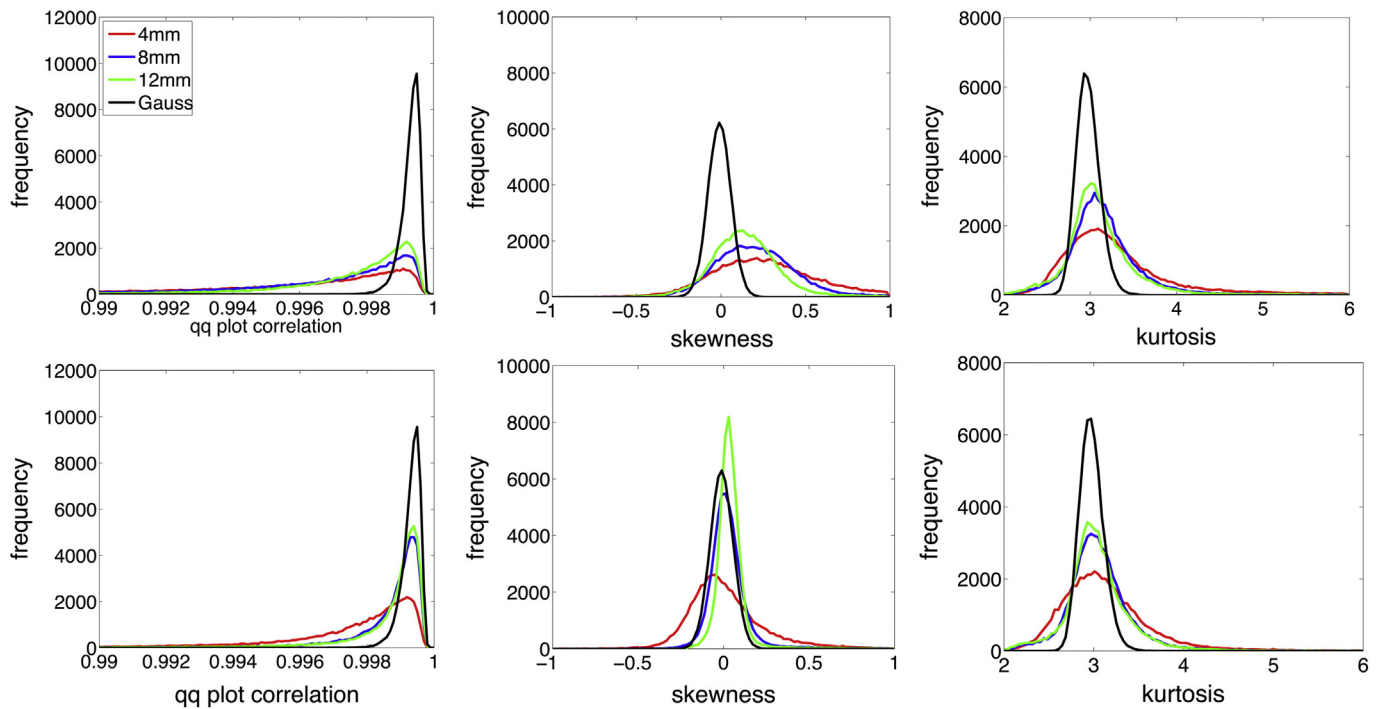


Fig. 5. Gaussianity of the residuals under the generative model of local gray matter volume using 1238 healthy adult subjects with ages 18–94 years and different degrees of smoothing, in particular applying Gaussian kernels of 4 (red), 8 (blue), and 12 (green) mm full width at half maximum (FWHM). Expected results under Gaussian assumptions are given in black. Top row shows residuals from untransformed data whereas the bottom row depicts voxelwise Box-Cox transformed data. (left) Histogram of Q–Q plot correlations of all voxels. (middle) Histogram of voxelwise sample estimates of skewness. (right) Histogram of voxelwise sample estimates of kurtosis.

which also provides an uncertainty for all locations in the input space. Notably, we observed a profound effect of variation of training sample size that indicated an increased predictive latent uncertainty in sparsely sampled locations of the covariate space in smaller samples, e.g. inspecting very old people, very large brains etc. We further aimed at prediction of local gray matter volume in the independent ADNI test sample of 100 healthy subjects. Fig. 7A shows the mean absolute error (MAE) of local predictions using GPs (left) in direct comparison to the general linear model (right). The MAE was found to be smaller using the GP model, especially in temporal and medial temporal lobe gray matter regions. In addition to the prediction error, an integral part of the proposed method is the predictive uncertainty. Thus, we also explored the effects of training sample size and data smoothness on predictive uncertainty. We found that the average uncertainty in test sample was rather independent of sample size, and that image smoothness induced noise differences had stronger effects (see Fig. 7B left). However, the predictive uncertainty for single case decisions strongly varied across subjects in the test sample when training GP models with smaller control samples (see Fig. 7B right).

In order to validate the GP-based z-scores for single case inference in subjects with dementia, we also assessed global and local z-scores (i.e. NPMs) in subjects with clinical indications for neuropathology, in particular with diagnosis of Mild Cognitive Impairment and Alzheimer's disease. Fig. 8A shows ADNI test sample z-scores for local gray matter volume in the hippocampus voxel (24, -12, -18 MNI) and global brain volumes after GP model training with the full healthy aging database. The average z-scores across the healthy controls were found to be close to zero. In contrast, clinical group subjects' revealed decreased z-scores in hippocampus voxel volume and total gray matter volume and increased z-scores of total cerebrospinal fluid volume. Irrespective of the substantial variability in healthy aging, the z-scores of test patient's suggest additional local hippocampus and global gray matter volume atrophy. Assuming that the diagnosis of the ADNI subjects is true, one can compare the efficiency of local and global z-scores with the conventional approach of t-test based single case inference. For the

particular purpose of comparison we applied Gaussian process classification to separate patients with pMCI and AD from controls only on the basis of the hippocampus voxel and the global volumes (Fig. 8B, see also Discussion). Fig. 8B middle column shows the receiver operating characteristic (ROC) curves and the area under curve (AUC) as performance metrics for the two dimensional classification using z-scores from hippocampus gray matter volume and one of the global brain parameters. Using local and global z-scores combined revealed a better classification performance in terms of AUC compared to the conventional t-value based separation on a subject by subject basis (Fig. 8B right column). Finally, in order to illustrate the proposed method, Fig. 9 summarizes model components and NPMs in 6 ADNI test subjects. Decreased z-scores are expected to emphasize local gray matter abnormalities due to atrophy or alternatively unknown covariate effects. Focal reductions of predictive probabilities were particularly observed in lateral and medial temporal lobe regions of many patients diagnosed with AD.

Discussion

Here we applied Gaussian process models for prediction and single case inference about local and global brain structural abnormalities in aging subjects. We implemented a non-parametric generative model of healthy aging, which allows individualized predictions in patients at risk of developing dementia. Using simulations we demonstrated advantages of the approach over existing methods for the purpose of prediction and inference in healthy and diseased subjects. As a further proof of concept, we focussed on real MRI data in a large healthy aging VBM database and tested the GP models to detect abnormalities in the most common neurodegenerative disease, AD. An accumulating body of work has demonstrated that medial temporal lobe atrophy is a consistent and pathologically verified (Burton et al., 2008) marker for AD (for review see Frisoni et al., 2010) which also has been shown to have the strongest effect sizes in direct comparison of controls and AD (Risacher et al., 2010). Medial temporal atrophy is also one of the MR-

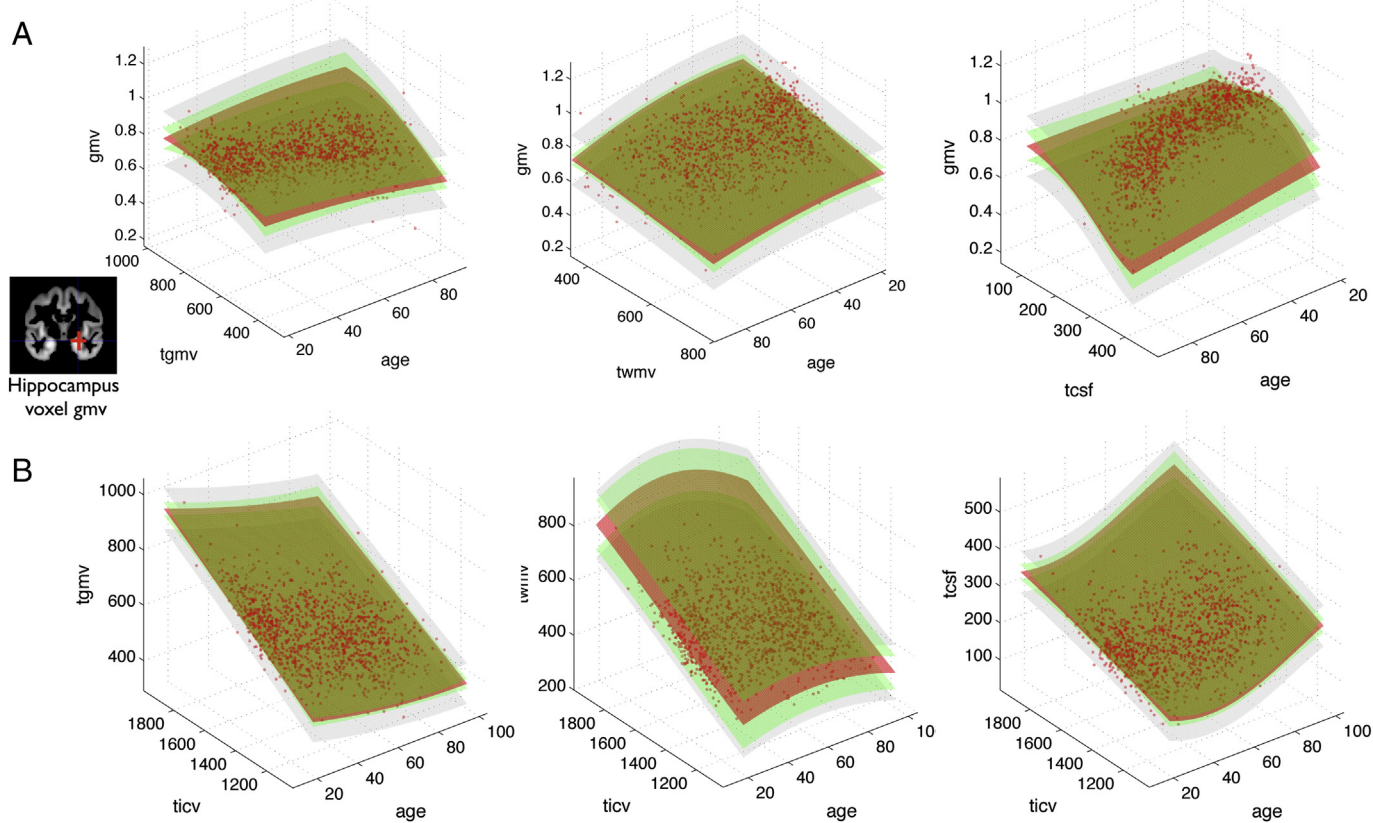


Fig. 6. Gaussian process models of local and global gray matter volume in the 1238 healthy subject sample. (A) Illustrates the GP based generative model of local GMV in a single voxel in hippocampus (24, -12, -18) mm MNI. Columns indicate the dependency on age and total gray matter volume (tgmv, left) total white matter volume (twmv, middle) and total cerebrospinal fluid volume (tcsl, right) respectively. Depicted are 3D surface plots of model components, continuously shown over test locations in input dimensions. Posterior distribution of latent variables $g(\mathbf{x}, \theta)$ with expectation \bar{g} (red) and standard deviation $\bar{g} \pm 1.96\text{std}(g)$ (green) is shown. The likelihood model standard deviations $\sigma = \text{std}(\epsilon)$ is shown as $\bar{g} \pm 1.96\sigma$ (gray). (B) Illustrates the GP based generative model of tgmv (left), twmv (middle) and tcsl (right). Columns indicate total intracranial volume (ticv) and age respectively.

670 based biomarkers discussed for revised definitions of AD (Dubois et al.,
671 2010; McKhann et al., 2011). Applying our GP model to the test samples,
672 we observed a considerable reduction of medial temporal lobe z-scores
673 in patients diagnosed with MCI and AD.

674 As suggested by related studies using parametric models (Salmond
675 et al., 2002; Scarpazza et al., 2013), we aimed at reducing potential
676 biases due to violations of normality assumptions of modulated VBM
677 data. As shown by Viviani et al. (2007), influences of non-normality
678 can be successfully reduced by appropriate transformation of the data.
679 Crucially, the deviations from normality do not follow a uniform pattern
680 across voxels, and thus we applied a voxel specific Box-Cox transformation
681 using a maximum likelihood method. By doing so, we observed a
682 substantial improvement of residuals' normality, which was further in-
683 creased by precedent application of 8 mm or 12 mm Gaussian smoothing
684 kernels. We found that the local GP model evidence was strongly
685 dominated by the variance of noise model, i.e. with lower residual var-
686 iance resulting in higher evidence. Note, however that the observed ev-
687 idence differences do not have the same meaning as in the context of
688 Bayesian model comparisons (see e.g. Penny, 2012) where one com-
689 pares different models of the same data rather than different models
690 of different data, e.g. from different voxels. Most cortical regions pro-
691 vided slightly smaller noise variances compared to subcortical regions
692 especially the thalamus and also the basal ganglia. These regional differ-
693 ences in the GP models might be due to effects of segmentation, nonlin-
694 ear normalization, the total explained variance by the covariate space,
695 and the true individual differences of local gray matter volume. There
696 was a further tendency to a slightly smaller amount of noise in fronto-
697 temporal compared to occipito-parietal gray matter regions which
698 might be related to the fact that age-related effects in elderly subject

699 brains are often found to be less emphasized in posterior brain regions 699 (Fjell and Walhovd, 2010; Raz and Rodriguez, 2006). 700

701 Earlier studies demonstrated that VBM and parametric models 701 afford inference about age-related gray matter volume differences in 702 healthy aging groups (Good et al., 2001; Hutton et al., 2009; Kennedy 703 et al., 2009; Ziegler et al., 2012b) and brain pathology in single patients 704 (Colliot et al., 2006; Mehta et al., 2003; Mühlau et al., 2009; Salmond 705 et al., 2003; Sehm et al., 2011). In addition, recent studies also showed 706 the potential of recognition models and multivariate classifiers to de- 707 code early stage diagnosis based on brain scans in dementia and espe- 708 cially AD (Adaszewski et al., 2013; Davatzikos et al., 2009, 2011; 709 Klöppel et al., 2008; Misra et al., 2009; Westman et al., 2011, 2012). Al- 710 though multivariate decoding models are expected to be powerful, sen- 711 sitive, and highly accurate, we argue that using only 'black box' schemes 712 might lack transparency and simplicity for decisions made in current 713 clinical practice. Therefore, our approach aimed at decision support in 714 the gap between multivariate classifiers (Klöppel et al., 2008) and qual- 715 itative visual inspection of scans (DeCarli et al., 2007; Korf et al., 2004). 716

717 A contribution of this paper is to apply a Bayesian approach that in-
718 corporates model- and predictive uncertainty for the single case infer-
719 ence. As recently emphasized by Klöppel et al. (2012), furnishing 720 predictive probabilities in clinical disease state classification tasks can 721 provide useful measures of the confidence for classification results. 722 This idea was also explored by Marquand et al. (2010) using GP classifi-
723 cation of whole brain patterns of brain activity in response to thermal 723 pain (see also Hahn et al., 2011). We extend these results to GP regres-
724 sion of continuous variables and show the potential value of predictive 725 probabilities to support clinician's decisions about gray matter abnor-
726 malities in aging subjects. We like to point out two interpretations. 727

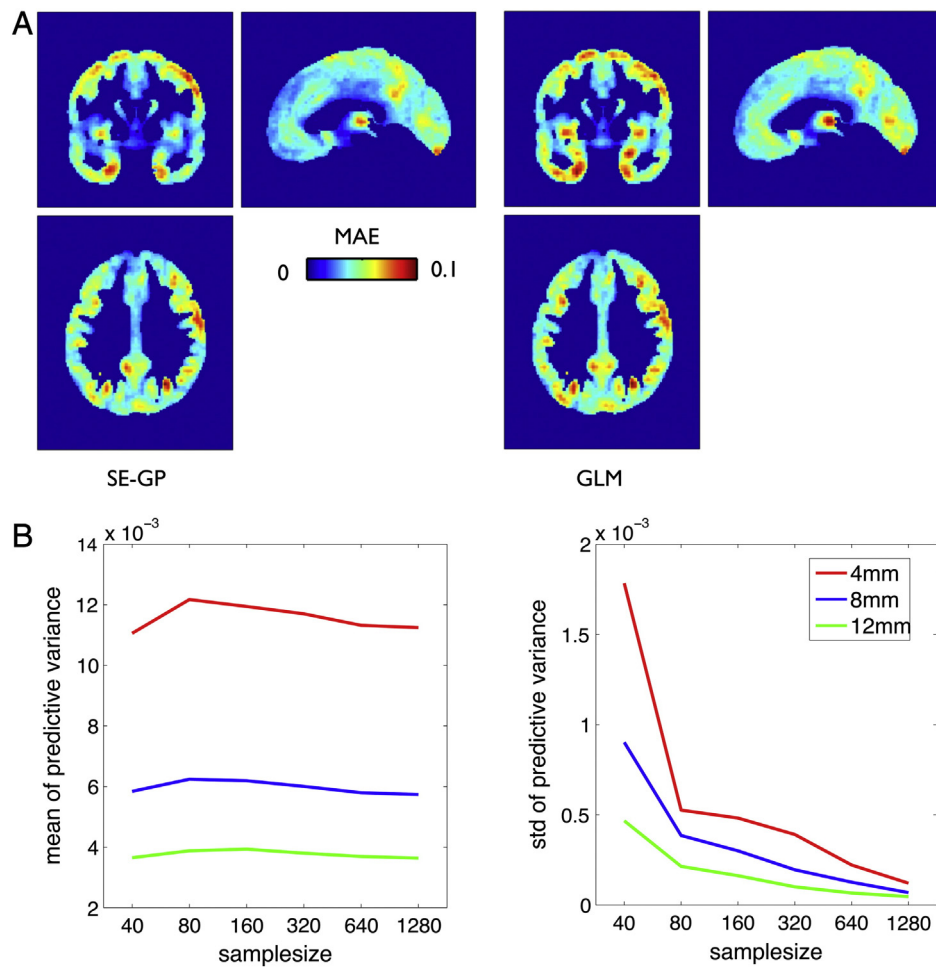


Fig. 7. Gaussian process model predictions in independent ADNI test sample of healthy subjects. (A) Mean absolute error of local predictions using squared exponential GP (left) based on subject's age, sex, global volumes, and type of scanner as input variables. For method comparison the predictions were repeated using the general linear model (GLM) estimates $B = (X' * X)^{-1} X' * Y$ of the all covariates X in the training sample for predictions $Y_t = X_t * B$ in the test sample. (B) Exploring the effects of training sample size on the predictive variance (uncertainty) u_{ij}^2 for predictions of hippocampal GMV at $(24, -12, -18)$ of the independent ADNI test sample. Random training subsamples of sizes 40, 80, 160, 320, 640 and 1280 were drawn and Gaussian kernels of 4 (red), 8 (blue), and 12 (green) mm full width at half maximum (FWHM) were applied. The local GP model optimization and ADNI healthy test sample predictions were repeated 20 times and the following parameters were averaged across these repetitions. The plots show the mean (left) and standard deviation (right) of the predictive uncertainty in the test sample. Increasing the training sample size mainly reduces the subject by subject variability of individual predictive uncertainty of the model.

Firstly, the presented z-scores from the local NPMs and global indices aim to support clinical inference about single patients' brain structure at risk of dementia. In analogy to neuropsychological test scores, by inspecting the NPM and the three global z-scores of a patient, the clinician is quantitatively and transparently informed about the patient's brain volumes in relation to a large healthy reference sample. At the same time the approach accounts for the effects of important covariates and individual differences aging. Increasingly negative z-scores indicate an increased risk of local and global atrophy. Secondly, NPMs can be seen as part of a naive Bayesian inference, which clinical experts might follow when judging scans about alternative causes of atrophy in an individual patient at risk of developing dementia. Thus, to support inference about several causes, the NPMs of $P(\text{scan}|\text{healthy})$ might be complemented by specific disease likelihood maps, e.g. $P(\text{scan}|AD)$ for Alzheimer's disease. The latter could be similarly obtained from local GP based pathology models in the clinical populations of interest.

As recently pointed out, multivariate recognition of AD disease states (Dukart et al., 2011) and voxelwise generative models of AD disease progression (Dukart et al., 2013) should necessarily account for regionally inhomogeneous age-related baseline changes in healthy controls. Thus, considering this variability our trajectory model presents an appropriate reference for detection of gray matter abnormalities in early and late disease onset, e.g. in early-onset vs. late-onset AD. Moreover, it extends existing approaches by avoiding the limitations of low degree

polynomial expansions of age (see also Fjell et al., 2010). The shape of lower degree models is restrictive and imposes strong constraints on the unknown developmental process. This might reveal poor estimates of the structural trajectory in analyses spanning several decades of the lifespan. Although higher degree polynomials provide more flexibility of trajectory shape than lower degree polynomials, for our purpose of predictions we prefer a non-parametric GP covariance model which does not require additional model comparisons for the selection of different polynomial degrees. Note, that using a GP model has some formal correspondence to regularization problems using penalties on derivatives and also smoothing spline models (Wahba, 1990) can be seen as a special case of the GP framework (see e.g. Sections 6.2 and 6.3 in Rasmussen and Williams, 2006). In contrast to recent applications of smoothing splines and kernel estimators in structural neuroimaging, the GP framework applies Bayesian evidence based optimization of length scale parameters instead of using cross-validation procedures to specify the smoothness or kernel bandwidth parameters respectively. Note, that unlike polynomial models, a squared exponential GP covariance implements a local regression method, i.e. the local structural trajectory only depends on data points of subjects with similar ages. This is particularly useful for lifespan studies, where additional inclusion of older (younger) subjects might not be expected to change predictions for younger (older) participants respectively. Our approach has some similarity to outlier detection schemes, used for patient classification.

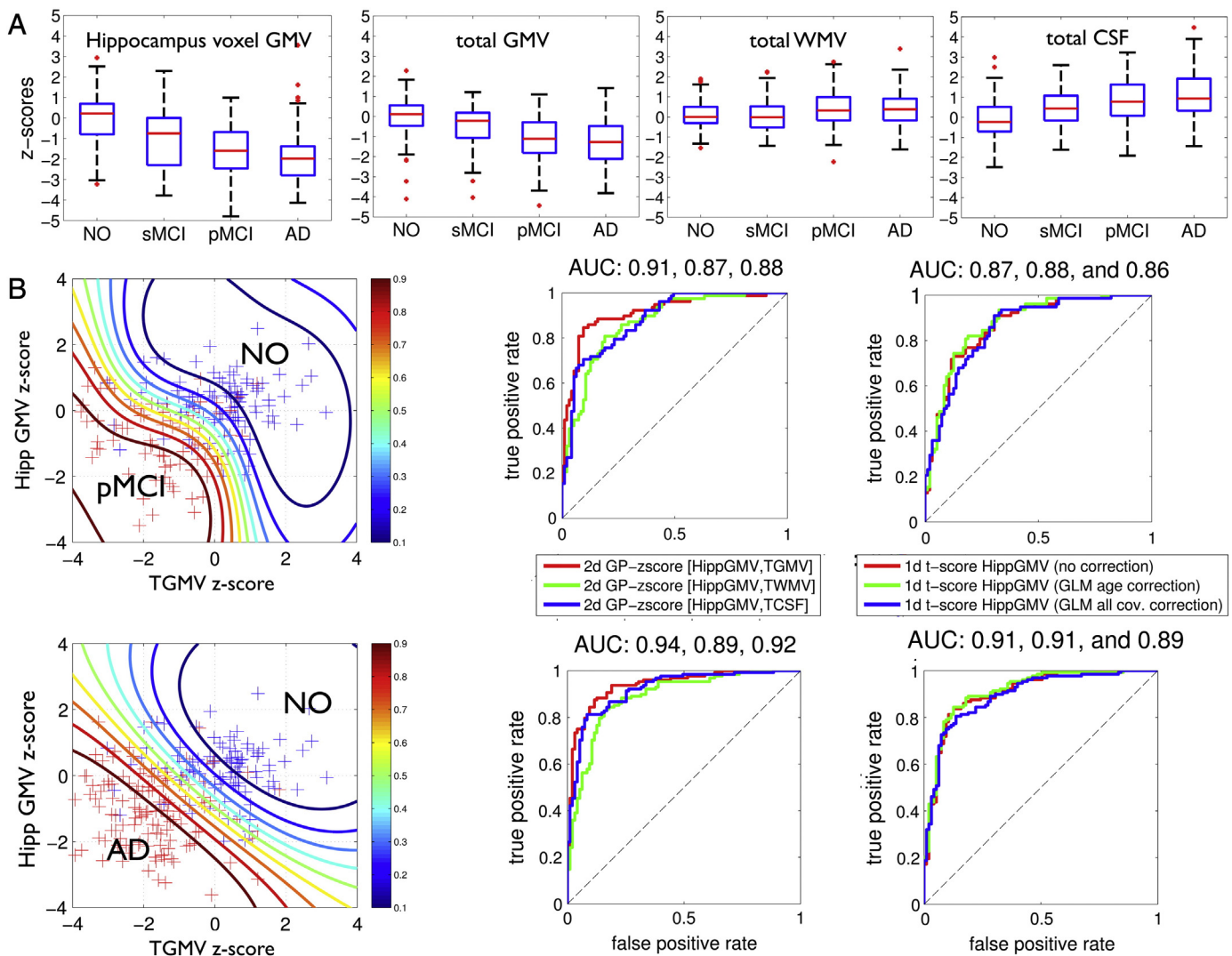


Fig. 8. Gaussian process model based z-scores of global and local volumes in the ADNI test sample. (A) First column shows z-scores of predictive probabilities δ_{ij} of hippocampal voxel GMV at (24, -12, -18) mm MNI of 415 scans from study participants with ages 55–93 years. Separate boxplots for 100 NO, 95 stable MCI (sMCI), 92 progressive MCI (pMCI), and 128 AD subjects subgroups are shown. Columns 2–4 depict z-scores for the GP model of global volumes. (B) Potential of GP-based local and global volume z-scores and comparison to t-test based single case inference. The left column shows a characterization of the pMCI and NO (top) and AD and NO (bottom) subjects in 2 dimensional plot using z-scores from a single hippocampus voxel GMV and total gray matter volume respectively. Additional contours show predictive probabilities obtained by post hoc Gaussian process classification of the clinical vs. normal subjects using a squared exponential covariance and cumulative Gaussian likelihood function. Middle column shows receiver operating characteristic (ROC) curves of classification of pMCI vs. NO (top) and AD vs. NO (bottom) using a 2D Gaussian process classification with leave one out cross-validation. Colors indicate 2D classification based on local gray matter volume with tgmv (red), twmv (blue), and tcsf (green) respectively. The right column shows the same group classification based on 1d Gaussian process classification of uncorrected t-values (red), t-values after age correction using general linear model (GLM) (blue), and t-values after GLM based correction of all covariate effects.

In a recent study Mourao-Miranda et al. (2011) addressed the problem of measuring departures from a distribution of Gaussian multivariate patterns of fMRI activity by modeling the boundary of this distribution.

It is important to note that we aimed to provide a map to support expert decisions about the current state of atrophy rather than to predict the subject's disease status per se. In contrast, we here address inference at the level of local and global gray matter volumes. The above presented classification of subjects based on local and global volumes was used to provide a proof of principle that GP z-scores might afford slightly more accurate characterization of individuals compared to existing methods. Otherwise, for the purpose of inference about the causes of atrophy, e.g. AD vs. MCI, AD vs. NO, etc., the whole pattern of features combining the NPM and global z-scores is expected to be more informative than single voxels and can be feed into supervised learning algorithms. We would also like to mention the commonalities and differences with the BrainAGE approach which was recently introduced by Franke et al. (2010). The author's multivariate age decoding scheme has shown potential applications for accurate predictions of conversion

of MCI to AD (Gaser et al., 2013). Both models, BrainAGE and NPMs exploit prediction errors under the assumption of a model of healthy brain aging and take advantage of the increased availability of healthy subject MRI data. However, the approaches also fundamentally differ with respect to the level of inference and treatment of individual differences. BrainAGE provides a whole brain pattern-based index of age-typical atrophy, whereas NPMs quantify normative expectation and confidence about local gray matter volumes. We therefore argue, that both approaches provide complementary and potentially useful information about a single elderly patient's brain. In contrast to the application of multivariate classifiers (for review Klöppel et al., 2012) the integration of likelihood and priors is still performed by a clinician himself. The benefit of this approach though can only be verified in clinical settings using this technique in direct comparison with visual inspection of structural MRI scans in native space. Notably, native space T1 scan inspection provides qualitative in contrast to quantitative information about the atrophy in single cases. Moreover, the prior knowledge accumulated over years of clinical experience is still expected to reflect smaller sample

group	NO	NO	NO	AD	AD	AD
rid	130	813	19	760	1373	7
age	73.16	72.82	73.19	69.46	75.48	75.48
sex	male	male	female	female	male	male
tgmv	690	630	546	537	408	576
ticv	1614	1450	1277	1273	1213	1271

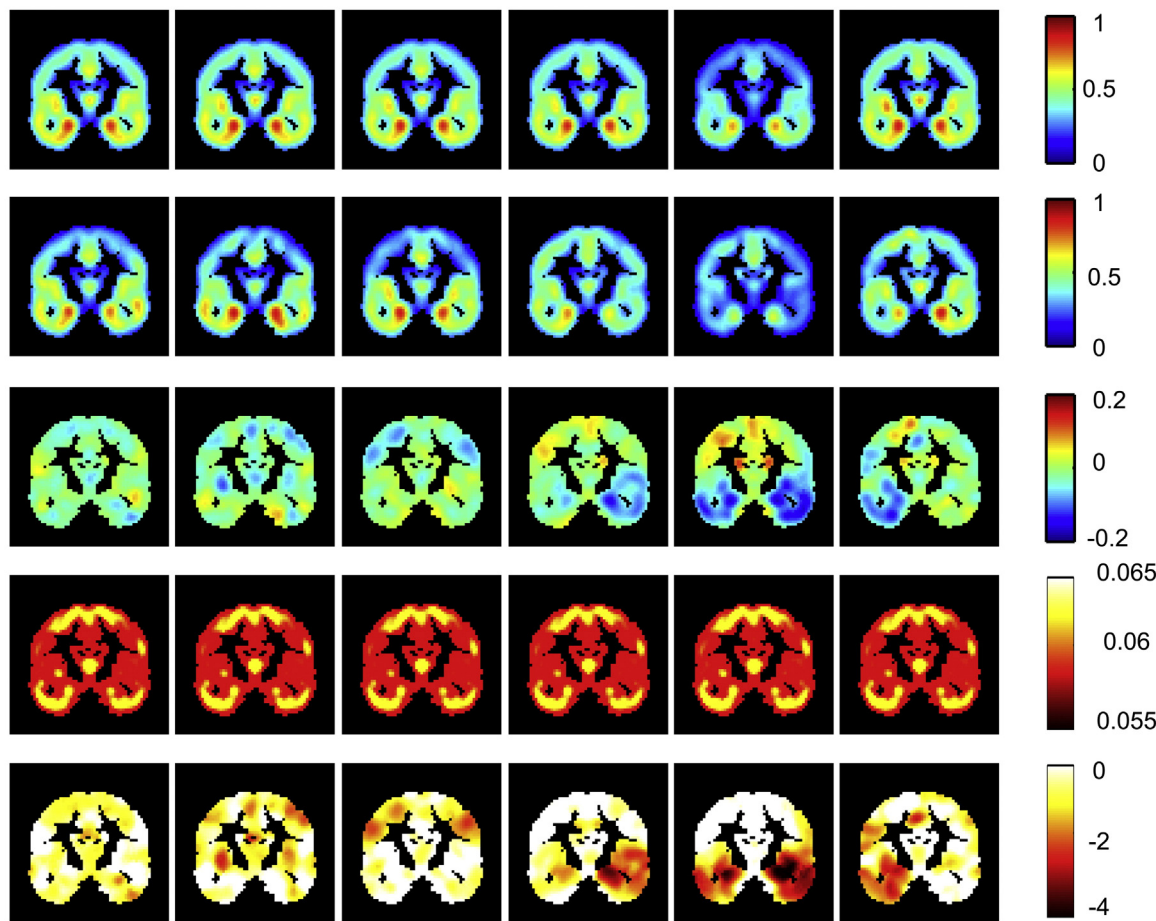


Fig. 9. Model components and Normative Probability Maps (NPMs) for 3 NO and 3 AD subjects from the ADNI testing sample in coronal slice and 12 mm full width at half maximum (FWHM) data. Individual ADNI grids, age, sex, total gray matter volume (ml) and total intracranial volume (ml) are given. Descending rows show the prediction by the GP model, the observed local gray matter volumes, prediction errors (i.e. observed–expected values), the square root of predictive uncertainty and NPMs (i.e. local z-maps).

sizes than the 1238 subjects. However, at the moment we can only speculate that clinicians who additionally inspect the quantitative model based NPMs and three global z-scores might come to more valid clinical conclusions facing patients with different brain sizes, sex, and up to five decades of age differences. Further validation studies might address the comparison of qualitative and quantitative single case inference schemes in clinical settings.

In order to facilitate applications in other samples, we explored the effects of image smoothness and sample size for our GP model and individualized predictions, especially the predictive uncertainty. Using large smoothing kernels for VBM data, a higher validity of statistical tests is achieved at the expense of the fine-grained structure of the cortical mantle (Viviani et al., 2007). We observed that stronger smoothing consistently reduced the local and the whole brain average GP model noise variance. The noise level has a substantial contribution to the variance of the predictive distribution. Thereby, predicting local gray matter volume in single subjects of the ADNI test data, we observed that stronger smoothing reduced uncertainty. Note, by using z-scores of the predictive distribution to obtain the NPMs, the uncertainty differences are expected to affect the sensitivity to detect local abnormalities. For instance, larger absolute gray matter reductions would be necessary to produce the same z-score reductions (in the NPM) within two voxels with high compared to low predictive uncertainty. Although this

might introduce differences in the NPMs across different voxels, this is a desired behavior of the model and renders inferences about local gray matter volumes more valid. Regarding the question of a sufficient adult control sample size for valid predictions in test subjects, we observed more consistent hyperparameters and latent variable estimates by training with larger subsamples of our database. Similar to parametric models, larger random training subsamples were also found to better capture potential late-life nonlinearities and accelerated structural decline (Fjell et al., 2012; Ziegler et al., 2012b), which then affords more specific predictions in subjects at risk for developing dementia. Note, that using the presented covariance kernel forms an information bottleneck that compresses individual differences in the covariate space to one kernel matrix for subsequent predictions. Consequently, using larger training samples also results in more densely sampled covariate spaces which afford more precise individualized predictions. Inspecting test subjects' hippocampus predictions using a training database of increasing size, we found a rather constant average uncertainty of predictions but substantially reduced fluctuation of precision across individual test subjects. According to this analysis, a larger sample size favors a higher stability of the predictive uncertainty which is expected to result in a more constant sensitivity to detect brain abnormalities across different individuals, e.g. with different ages, brain sizes, etc. Note, however, that due to the domination of the noise term in the predictive

uncertainty, the effects of different degrees of smoothing and variability across the cortical mantle, is expected to be more substantial than fluctuations due to individual differences in very large samples.

Some caveats and directions for development of the presented approach have to be mentioned. Firstly, structural brain aging is expected to be a highly individual process embedded in a complex and reciprocally interacting system including the genes, physiology, behavior, and the individual cultural environment (Baltes et al., 2006; Jagust, 2009). We assume that this process becomes manifest in the individual brain trajectories forming a flowfield of lifespan brain development after accounting for subject's covariates. This is in line with recent evidence from mixed-effects analysis of repeated measures MRI, showing substantial individual differences of regional structural trajectories (Raz et al., 2010). Thereby, defining a sufficient normative reference for pathological structural aging, one necessarily requires an approximation of the structure of the flowfield including the most common individual differences. Apart from potential secular trends and cohort effects of a purely cross-sectional design (for a more detailed discussion of this point see Ziegler et al., 2012a) we here make the strong assumption that the hidden causes of individual differences in elderly are fully captured by the above considered covariate space \mathcal{D} . As recently pointed out by Doyle et al. (2013b), personalized modeling approaches are required in order to make personalized medicine reality. We might speculate that using a sufficiently high-dimensional multivariate parametrization of individual differences including genes, education, cognitive scores (see e.g. Ziegler et al., 2013), and behavior, the considered cross-sectional trajectory estimates might converge to estimates from repeated measures MRI design. Otherwise, combining cross-sectional with high quality longitudinal segmentations (Jovicich et al., 2013, see e.g.) might further improve model-based predictions and inference.

Secondly, a limitation of this study is the potential adverse effects of pooling across MRI scanners and sequences (Jovicich et al., 2013, see e.g.). However, the purpose of the proposed database-based prediction and inference in elderly subjects is to aim at generalization to new clinical scanners while exploiting the benefits of a large healthy aging reference sample and the diverse appearance of normal aging. In this particular model, local and global scanner effects are expected to be captured by increases of the model error variance. Within the Bayesian inference framework, we expect this to result in reduced predictive confidence for particular brain regions with expectable high scanner related artifacts, e.g. in subcortical regions. The proposed z-scores account for this local increase of uncertainty in terms of higher deviation from normality to be required to observe the same z-score. Thus, the gains of generalization to new clinical scanners come at the cost of a reduced sensitivity for gray matter abnormality detection. Notably, an alternative model accounting for all site effects is likely to result in biased conclusions in predictions on new scanners due to severe overconfidence. We argue that the provided comparisons of GP-based z-scores in clinical groups still demonstrate a potentially useful characterization of unseen subjects from new scanners. Future studies might focus on generalizable assumptions about forms of scanner related variability which could be included in model training and inform predictions on scanners with specific imaging parameters.

Thirdly, a serious problem with GP methods is that it requires computation which grows as $O(n^3)$, where n is the number of subjects. This computation is very expensive, especially if we aim at the advantages of large sample healthy aging databases. Future studies might explore sparse approximation techniques (Quiñonero-Candela and Rasmussen, 2005; Quiñonero-Candela et al., 2007) for more effective local models or spatial regularization (see e.g. Banerjee et al., 2008; Sang and Huang, 2012).

Finally, the local brain morphology in our GP models was restricted to gray matter segments obtained from VBM. Although medial temporal

lobe atrophy is one of the most-established imaging biomarkers for AD (Frisoni et al., 2010; Teipel et al., 2013), our GP framework might be extended to other potential disease sensitive sequences and modalities, e.g. local white matter hyperintensities (Brickman et al., 2012; Carmichael et al., 2010) or [¹⁸F]fluorodeoxyglucose Positron Emission Tomography (FDG-PET) (Dukart et al., 2013) as well as amyloid PET (Quigley et al., 2011).

Conclusion

931

We argue, that decisions about subjects at risk to convert to pathological aging might be supported via transparent evidence given the quantitative models of normal and pathological aging. Normative probability maps and global brain volume z-scores afford individualized detection of abnormalities and appropriately account for the uncertainty of the model and the model's predictions due to random influences, e.g. noisy observations and sampling.

Acknowledgments

939

We are grateful to Karl Friston, John Ashburner, Will Penny, and Thomas Hope for providing valuable comments and corrections to the manuscript. We are also grateful to Julian Karch, and Hannes Nickisch for insightful discussions and comments about the modeling framework. This work was supported by a fellowship within the Postdoc-Program of the German Academic Exchange Service (DAAD) and BMBF grant 01EV0709. Data collection and sharing for this project was funded by the Alzheimer's Disease Neuroimaging Initiative (ADNI) (National Institutes of Health Grant U01 AG024904). ADNI is funded by the National Institute on Aging, and the National Institute of Biomedical Imaging and Bioengineering, and through generous contributions from the following: Abbott; Alzheimer's Association; Alzheimer's Drug Discovery Foundation; Amorfix Life Sciences Ltd.; AstraZeneca; Bayer HealthCare; BioClinica, Inc.; Biogen Idec Inc.; Bristol-Myers Squibb Company; Eisai Inc.; Elan Pharmaceuticals Inc.; Eli Lilly and Company; F. Hoffmann-La Roche Ltd and its affiliated company Genentech, Inc.; GE Healthcare; Innogenetics, N.V.; Janssen Alzheimer Immunotherapy Research & Development, LLC; Johnson & Johnson Pharmaceutical Research & Development LLC; Medpace, Inc.; Merck & Co., Inc.; Meso Scale Diagnostics, LLC.; Novartis Pharmaceuticals Corporation; Pfizer Inc.; Servier; Synarc Inc.; and Takeda Pharmaceutical Company. The Canadian Institutes of Health Research is providing funds to support ADNI clinical sites in Canada. Private sector contributions are facilitated by the Foundation for the National Institutes of Health (www.fnih.org). The grantee organization is the Northern California Institute for Research and Education, and the study is coordinated by the Alzheimer's Disease Cooperative Study at the University of California, San Diego. ADNI data are disseminated by the Laboratory for Neuro Imaging at the University of California, Los Angeles. The Open Access Series of Imaging Studies (OASIS) is supported by grants P50 AG05681, P01 AG03991, R01 AG021910, P50 MH071616, U24 RR021382, and R01 MH56584.

970

Conflict of interest

971

The authors declare that there are neither actual nor potential conflicts of interest.

972

973

References

974

- Adaszewski, S., Dukart, J., Kherif, F., Frackowiak, R., Draganski, B., 2013. How early can we predict Alzheimer's disease using computational anatomy? *Neurobiol. Aging*. <http://dx.doi.org/10.1016/j.neurobiolaging.2013.06.015>.
- Ashburner, J., 2007. A fast diffeomorphic image registration algorithm. *NeuroImage* 38 (1), 95–113.
- Ashburner, J., Friston, K.J., 2000. Voxel-based morphometry—the methods. *NeuroImage* 11 (6 Pt 1), 805–821.
- Ashburner, J., Friston, K.J., 2005. Unified segmentation. *NeuroImage* 26 (3), 839–851.

984

- 985 Ashburner, J., Klöppel, S., 2011. Multivariate models of inter-subject anatomical variability. *NeuroImage* 56 (2), 422–439.
- 986 Baltes, P.B., Reuter-Lorenz, P.A., Rösler, F., 2006. Lifespan Development and the Brain. The
988 Perspective of Biocultural Co-constructivism. Cambridge University Press, New York.
- 989 Banerjee, S., Gelfand, A.E., Finley, A.O., Sang, H., 2008. Gaussian predictive process models
990 for large spatial data sets. *J. R. Stat. Soc. Ser. B (Stat Methodol.)* 70 (4), 825–848.
- 991 Box, G.E.P., Cox, D.R., 1964. An analysis of transformations. *J. R. Stat. Soc. Ser. B (Stat
992 Methodol.)* 26 (2), 211–252.
- 993 Brickman, A.M., Provenzano, F.A., Muraskin, J., Manly, J.J., Blum, S., Apa, Z., Stern, Y.,
994 Brown, T.R., Luchsinger, J.A., Mayeux, R., 2012. Regional white matter hyperintensity
995 volume, not hippocampal atrophy, predicts incident Alzheimer disease in the community.
996 *Arch. Neurol.* 69 (12), 1621–1627.
- 997 Burton, E.J., Barber, R., Mukaeova-Ladinska, E.B., Robson, J., Perry, R.H., Jaros, E.,
998 Kalaria, R.N., O'Brien, J.T., 2008. Medial temporal lobe atrophy on MRI differentiates
999 Alzheimer's disease from dementia with Lewy bodies and vascular cognitive
1000 impairment: a prospective study with pathological verification of diagnosis.
Brain 132 (1), 195–203.
- 1001 Carmichael, O., Schwarz, C., Drucker, D., Fletcher, E., Harvey, D., Beckett, L., Jack, C.R.,
1002 Weiner, M., DeCarli, C., the Alzheimer Disease Neuroimaging Initiative, 2010. Longitudinal
1003 changes in white matter disease and cognition in the first year of the Alzheimer
1004 disease neuroimaging initiative. *Arch. Neurol.* 67 (11), 1370–1378.
- 1005 Colliot, O., Bernasconi, N., Khalili, N., Antel, S.B., Naessens, V., Bernasconi, A., 2006. Individual
1006 voxel-based analysis of gray matter in focal cortical dysplasia. *NeuroImage* 29 (1),
1007 162–171.
- 1008 Crawford, J.R., Garthwaite, P.H., 2012. Single-case research in neuropsychology: a comparison
1009 of five forms of t-test for comparing a case to controls. *Cortex* 48 (8), 1009–1016.
- 1010 Crawford, J.R., Howell, D.C., 1998. Comparing an individual's test score against norms derived
1011 from small samples. *Clin. Neuropsychol.* 12 (4), 482–486.
- 1012 Cuadra, M.B., Cammoun, L., Butz, T., Cuisenaire, O., Thiran, J.P., 2005. Comparison and validation
1013 of tissue modelization and statistical classification methods in T1-weighted MR brain images.
IEEE Trans. Med. Imaging 24 (12), 1548–1565.
- 1014 Davatzikos, C., Xu, F., An, Y., Fan, Y., Resnick, S.M., 2009. Longitudinal progression of
1015 Alzheimer's-like patterns of atrophy in normal older adults: the SPARE-AD index.
Brain 132 (Pt 8), 2026–2035.
- 1016 Davatzikos, C., Bhatt, P., Shaw, L.M., Batmanghelich, K.N., Trojanowski, J.Q., 2011. Prediction
1017 of MCI to AD conversion, via MRI, CSF biomarkers, and pattern classification.
Neurobiol. Aging 32 (12), 2322 (e19–27).
- 1018 DeCarli, C., Frisoni, G.B., Clark, C.M., Harvey, D., 2007. JAMA Network | JAMA Neurology |
1019 Qualitative estimates of medial temporal atrophy as a predictor of progression from
1020 mild cognitive impairment to dementia. *Arch. Neurol.* 64 (1), 108–115.
- 1021 Doyle, O.M., Ashburner, J., Zelaya, F.O., Williams, S.C.R., Mehta, M.A., Marquand, A.F.,
1022 2013a. Multivariate decoding of brain images using ordinal regression. *NeuroImage*
81 (1), 347–357.
- 1023 Doyle, O.M., Tsaneva-Atanasova, K., Harte, J., Tiffin, P.A., Tino, P., Díaz-Zuccarini, V., 2013b.
Bridging paradigms: hybrid mechanistic-discriminative predictive models. *IEEE
Trans. Biomed. Eng.* 60 (3), 735–742.
- 1024 Dubois, B., Feldman, H.H., Jacova, C., Cummings, J.L., 2010. Revising the definition of
1025 Alzheimer's disease: a new lexicon. *Lancet Neurol.* 9 (11), 1118–1127.
- 1026 Dukart, J., Schroeter, M.L., Mueller, K., the Alzheimer Disease Neuroimaging Initiative,
1027 2011. Age correction in dementia – matching to a healthy brain. *PLoS One* 6 (7), e22193.
- 1028 Dukart, J., Kherif, F., Mueller, K., Adaszewski, S., Schroeter, M.L., Frackowiak, R.S.J.,
1029 Draganski, B., Alzheimer Disease Neuroimaging Initiative, 2013. Generative FDG-PET and MRI model of aging and disease progression in Alzheimer's disease. *PLoS
Comput. Biol.* 9 (4), e1002987.
- 1030 Fjell, A.M., Walhovd, K.B., 2010. Structural brain changes in aging: courses, causes and
1031 cognitive consequences. *Rev. Neurosci.* 21 (3), 187–221.
- 1032 Fjell, A.M., Walhovd, K.B., Westlye, L.T., Østby, Y., Tamnes, C.K., Jernigan, T.L., Gamst, A.,
1033 Dale, A.M., 2010. When does brain aging accelerate? Dangers of quadratic fits in
1034 cross-sectional studies. *NeuroImage* 50 (4), 1376–1383.
- 1035 Fjell, A.M., Westlye, L.T., Grydeland, H., Amlie, I., Espeseth, T., Reinvang, I., Raz, N., Dale,
1036 A.M., Walhovd, K.B., Alzheimer Disease Neuroimaging Initiative, 2012. Accelerating
1037 cortical thinning: unique to dementia or universal in aging? *Cereb. Cortex*. <http://dx.doi.org/10.1093/cercor/bhs379>.
- 1038 Fjell, A.M., Westlye, L.T., Grydeland, H., Amlie, I., Espeseth, T., Reinvang, I., Raz, N., Holland,
1039 D., Dale, A.M., Walhovd, K.B., the Alzheimer Disease Neuroimaging Initiative, 2013. Critical ages in the life course of the adult brain: nonlinear subcortical
1040 aging. *Neurobiol. Aging* 34 (10), 2239–2247.
- 1041 Franke, K., Ziegler, G., Klöppel, S., Gaser, C., the Alzheimer Disease Neuroimaging Initiative,
1042 2010. Estimating the age of healthy subjects from T1-weighted MRI scans using
1043 kernel methods: exploring the influence of various parameters. *NeuroImage* 50
1044 (3), 883–892.
- 1045 Frisoni, G.B., Fox, N.C., Jack, C.R., Scheltens, P., Thompson, P.M., 2010. The clinical use of
1046 structural MRI in Alzheimer disease. *Nat. Rev. Neurol.* 6 (2), 67–77.
- 1047 Friston, K.J., Ashburner, J., 2004. Generative and recognition models for neuroanatomy.
NeuroImage 23 (1), 21–24.
- 1048 Friston, K., Chu, C., Mourao-Miranda, J., Hulme, O., Rees, G., Penny, W., Ashburner, J., 2008.
Bayesian decoding of brain images. *NeuroImage* 39 (1), 181–205.
- 1049 Gaser, C., Franke, K., Klöppel, S., Koutsouleris, N., Sauer, H., the Alzheimer Disease
1050 Neuroimaging Initiative, 2013. BrainAGE in mild cognitive impaired patients:
1051 predicting the conversion to Alzheimer's disease. *PLoS One* 8 (6), e67346.
- 1052 Good, C.D., Johnsrude, I.S., Ashburner, J., Henson, R.N., Friston, K.J., Frackowiak, R.S., 2001.
A voxel-based morphometric study of ageing in 465 normal adult human brains.
NeuroImage 14 (1 Pt 1), 21–36.
- 1053 Groves, A.R., Chappell, M.A., Woolrich, M.W., 2009. Combined spatial and non-spatial
1054 prior for inference on MRI time-series. *NeuroImage* 45 (3), 795–809.
- 1055 Hahn, T., Marquand, A.F., Ehli, A.-C., Dresler, T., Kittel-Schneider, S., Jarczok, T.A., Lesch,
1056 K.-P., Jakob, P.M., Mourao-Miranda, J., Brammer, M.J., Fallgatter, A.J., 2011. Integrating
1057 neurobiological markers of depression. *Arch. Gen. Psychiatry* 68 (4), 361–368.
- 1058 Hope, T.M.H., Seghier, M.L., Leff, A.P., Price, C.J., 2013. Predicting outcome and recovery
1059 after stroke with lesions extracted from MRI images. *NeuroImage Clin.* 2, 424–433.
- 1060 Hutton, C., Draganski, B., Ashburner, J., Weiskopf, N., 2009. A comparison between voxel-
1061 based cortical thickness and voxel-based morphometry in normal aging. *NeuroImage*
48 (2), 371–380.
- 1062 Jagust, W., 2009. Imaging the Aging Brain. Oxford University Press, USA.
- 1063 Jovicich, J., Marizzoni, M., Sala-Llonch, R., Bosch, B., Bartrés-Faz, D., Arnold, J., Benninghoff,
1064 J., Wiltfang, J., Roccatagliata, L., Nobili, F., Hensch, T., Tränkner, A., Schönknecht, P.,
1065 Leroy, M., Lopes, R., Bordet, R., Chanoine, V., Ranjeva, J.-P., Didic, M., Gros-Dagnac,
1066 H., Payoux, P., Zoccatelli, G., Alessandrini, F., Beltramello, A., Bargalló, N., Blin, O.,
1067 Frisoni, G.B., PharmaCog Consortium, 2013. Brain morphometry reproducibility in
1068 multi-center 3 T MRI studies: a comparison of cross-sectional and longitudinal seg-
1069 mentations. *NeuroImage* 83, 472–484.
- 1070 Kennedy, K.M., Erickson, K.I., Rodrigue, K.M., Voss, M.W., Colcombe, S.J., Kramer, A.F.,
1071 Acker, J.D., Raz, N., 2009. Age-related differences in regional brain volumes: a com-
1072 parison of optimized voxel-based morphometry to manual volumetry. *Neurobiol.
Aging* 30 (10), 1657–1676.
- 1073 Kim, H., Ghahramani, Z., 2006. Bayesian Gaussian process classification with the EM-EP
1074 algorithm. *IEEE Trans. Pattern Anal. Mach. Intell.* 28 (12), 1948–1959.
- 1075 Klöppel, S., Stonnington, C.M., Chu, C., Draganski, B., Sciahill, R.I., Rohrer, J.D., Fox, N.C., Jack,
1076 C.R., Ashburner, J., Frackowiak, R.S.J., 2008. Automatic classification of MR scans in
1077 Alzheimer's disease. *Brain* 131 (Pt 3), 681–689.
- 1078 Klöppel, S., Abdulkadir, A., Jack, C.R., Koutsouleris, N., Mourão-Miranda, J., Vemuri, P.,
1079 2012. Diagnostic neuroimaging across diseases. *NeuroImage* 61 (2), 457–463.
- 1080 Korf, E.S.C., Wahlund, L.-O., Visser, P.J., Scheltens, P., 2004. Medial temporal lobe atrophy
1081 on MRI predicts dementia in patients with mild cognitive impairment. *Neurology*
63 (1), 94–100.
- 1082 Macke, J.H., Gerwinn, S., White, L.E., Kaschube, M., Bethge, M., 2011. Gaussian process
1083 methods for estimating cortical maps. *NeuroImage* 56 (2), 570–581.
- 1084 Maguire, E.A., Kumaran, D., Hassabis, D., Kopelman, M.D., 2010. Autobiographical memory
1085 in semantic dementia: a longitudinal fMRI study. *Neuropsychologia* 48 (1), 123–136.
- 1086 Marcus, D.S., Wang, T.H., Parker, J., Csernansky, J.G., Morris, J.C., Buckner, R.L., 2007. Open
1087 Access Series of Imaging Studies (OASIS): cross-sectional MRI data in young, middle
1088 aged, nondemented, and demented older adults. *J. Cogn. Neurosci.* 19 (9), 1498–1507.
- 1089 Marquand, A., Howard, M., Brammer, M., Chu, C., Coen, S., Mourao-Miranda, J., 2010. Quantitative
1090 prediction of subjective pain intensity from whole-brain fMRI data using Gaussian processes.
NeuroImage 49 (3), 2178–2189.
- 1091 McIntosh, R.D., Brooks, J.L., 2011. Current tests and trends in single-case neuropsychology.
Cortex 47 (10), 1151–1159.
- 1092 McKhann, G.M.G., Knopman, D.S.D., Chertkow, H.H., Hyman, B.T.B., Jack, C.R.C., Kawas, C.,
1093 H.C., Klunk, W.E.W., Koroshetz, W.J.W., Manly, J.J., Mayeux, R.R., Mohs, R.C.R., Morris,
1094 J.C.J., Rossor, M.N.M., Scheltens, P.P., Carrillo, M.C.M., Thies, B.B., Weintraub, S.S.,
1095 Phelps, C.H.C., 2011. The diagnosis of dementia due to Alzheimer's disease: recommendations
1096 from the National Institute on Aging—Alzheimer's Association workgroups on diagnostic guidelines
1097 for Alzheimer's disease. *Alzheimers Dement.* 7 (3), 7.
- 1098 Mechelli, A., Price, C.J., Friston, K.J., Ashburner, J., 2005. Voxel-based morphometry of the
1099 human brain: methods and applications. *Curr. Med. Imaging Rev.* 1 (1), 1–9.
- 1100 Migliaccio, R., Agosta, F., Toba, M.N., Samri, D., Corlier, F., de Souza, L.C., Chupin, M.,
1101 Sharman, M., Gorno-Tempini, M.L., Dubois, B., Filippi, M., Bartolomeo, P., 2012. Brain
1102 networks in posterior cortical atrophy: a single case tractography study and literature review.
Cortex 48 (10), 1298–1309.
- 1103 Misra, C., Fan, Y., Davatzikos, C., 2009. Baseline and longitudinal patterns of brain atrophy
1104 in MCI patients, and their use in prediction of short-term conversion to AD: results
1105 from ADNI. *NeuroImage* 44 (4), 1415–1422.
- 1106 Mourao-Miranda, J., Hardoon, D.R., Hahn, T., Marquand, A.F., Williams, S.C.R., Shawe-
1107 Taylor, J., Brammer, M., 2011. Patient classification as an outlier detection problem:
1108 an application of the one-class support vector machine. *NeuroImage* 58 (3), 793–804.
- 1109 Munes, M., Biswal, B.B., Castellanos, F.X., Milham, M.P., 2013. Making data sharing work:
1110 the FCP/INDI experience. *NeuroImage* 82, 683–691.
- 1111 Migliaccio, R., Agosta, F., Toba, M.N., Samri, D., Corlier, F., de Souza, L.C., Chupin, M.,
1112 Sharman, M., Gorno-Tempini, M.L., Dubois, B., Filippi, M., Bartolomeo, P., 2012. Brain
1113 networks in posterior cortical atrophy: a single case tractography study and literature review.
Cortex 48 (10), 1298–1309.
- 1114 Misra, C., Fan, Y., Davatzikos, C., 2009. Baseline and longitudinal patterns of brain atrophy
1115 in MCI patients, and their use in prediction of short-term conversion to AD: results
1116 from ADNI. *NeuroImage* 44 (4), 1415–1422.
- 1117 Mourao-Miranda, J., Almeida, J.R., Hassel, S., de Oliveira, L., Versace, A., Marquand, A.F.,
1118 Sato, J.R., Brammer, M., Phillips, M.L., 2012. Pattern recognition analyses of brain activation
1119 elicited by happy and neutral faces in unipolar and bipolar depression. *Bipolar
Disord.* 14 (4), 451–460.
- 1120 Mueller, S.G., Weiner, M.W., Thal, L.J., Petersen, R.C., Jack, C.R., Jagust, W., Trojanowski, J.Q.,
1121 Toga, A.W., Beckett, L., 2005. Ways toward an early diagnosis in Alzheimer's disease:
1122 the Alzheimer's Disease Neuroimaging Initiative (ADNI). *Alzheimers Dement.* 1 (1), 55–66.
- 1123 Mühlau, M., Wohlschläger, A.M., Gaser, C., Valet, M., Weindl, A., Nunnemann, S.,
1124 Peinemann, A., Etgen, T., Ilg, R., 2009. Voxel-based morphometry in individual patients:
1125 a pilot study in early Huntington disease. *AJNR Am. J. Neuroradiol.* 30 (3), 539–543.
- 1126 Mummery, C.J., Patterson, K., Price, C.J., Ashburner, J., Frackowiak, R.S., Hodges, J.R., 2000.
1127 A voxel-based morphometry study of semantic dementia: relationship between tempo-
1128 ral lobe atrophy and semantic memory. *Ann. Neurol.* 47 (1), 36–45.
- 1129 Neal, R.M., 1996. Bayesian Learning for Neural Network. Springer, New York.
- 1130 Peele, J.E., Cusack, R., Henson, R.N.A., 2012. Adjusting for global effects in voxel-based
1131 morphometry: gray matter decline in normal aging. *NeuroImage* 60 (2), 1503–1516.
- 1132 Penny, W.D., 2012. Comparing dynamic causal models using AIC, BIC and free energy.
1133 *NeuroImage* 59 (1), 319–330.

- 1157 Pyka, M., Hahn, T., Heider, D., Krug, A., Sommer, J., Kircher, T., Jansen, A., 2012. Baseline Ac-
1158 tivity Predicts Working Memory Load of Preceding Task Condition. *HBM*. [http://dx.
1159 doi.org/10.1002/hbm.22121](http://dx.doi.org/10.1002/hbm.22121).
- 1160 Quigley, H.H., Colloby, S.J.S., O'Brien, J.T.J., 2011. PET imaging of brain amyloid in
1161 dementia: a review. *Int. J. Geriatr. Psychiatry* 26 (10), 991–999.
- 1162 Quiñonero-Candela, J., Rasmussen, C.E., 2005. A unifying view of sparse approximate
1163 Gaussian process regression. *J. Mach. Learn. Res.* 6, 1939–1959.
- 1164 Quiñonero-Candela, J., Rasmussen, C.E., Williams, C.K.I., 2007. Approximation methods for
1165 Gaussian process regression. Technical Report MSR-TR-2007-124. Microsoft Research,
1166 Microsoft Corporation (<http://www.research.microsoft.com>).
- 1167 Rajapakse, J.C., Giedd, J.N., Rapoport, J.L., 1997. Statistical approach to segmentation
1168 of single-channel cerebral MR images. *IEEE Trans. Med. Imaging* 16 (2), 176–186.
- 1169 Rasmussen, C.E., 1996. Evaluation of Gaussian Processes and Other Methods for Non-
1170 linear Regression. (PhD thesis) Dept. of Computer Science, Univ. of Toronto, Toronto.
- 1171 Rasmussen, C.E., Williams, C.K.I., 2006. Gaussian Processes for Machine Learning. MIT
1172 Press, Cambridge.
- 1173 Raz, N., Rodriguez, K.M., 2006. Differential aging of the brain: patterns, cognitive correlates
1174 and modifiers. *Neurosci. Biobehav. Rev.* 30 (6), 730–748.
- 1175 Raz, N., Lindenberger, U., Rodriguez, K.M., Kennedy, K.M., Head, D., Williamson, A.,
1176 Dahle, C., Gerstorf, D., Acker, J.D., 2005. Regional brain changes in aging healthy
1177 adults: general trends, individual differences and modifiers. *Cereb. Cortex* 15
1178 (11), 1676–1689.
- 1179 Raz, N., Ghisletta, P., Rodriguez, K.M., Kennedy, K.M., Lindenberger, U., 2010. Trajectories of
1180 brain aging in middle-aged and older adults: regional and individual differences.
1181 *NeuroImage* 51 (2), 501–511.
- 1182 Risacher, S.L., Shen, L., West, J.D., Kim, S., McDonald, B.C., Beckett, L.A., Harvey, D.J., Jack, C.
1183 R., Weiner, M.W., Saykin, A.J., the Alzheimer Disease Neuroimaging Initiative, 2010.
1184 Longitudinal MRI atrophy biomarkers: relationship to conversion in the ADNI cohort.
1185 *Neurobiol. Aging* 31 (8), 1401–1418.
- 1186 Salimi-Khorshidi, G., Nichols, T.E., Smith, S.M., Woolrich, M.W., 2011. Using Gaussian-
1187 process regression for meta-analytic neuroimaging inference based on sparse obser-
1188 vations. *IEEE Trans. Med. Imaging* 30 (7), 1401–1416.
- 1189 Salmon, C.H., Ashburner, J., Vargha-Khadem, F., Connelly, A., Gadian, D.G., Friston, K.J.,
1190 2002. Distributional assumptions in voxel-based morphometry. *NeuroImage* 17 (2),
1191 1027–1030.
- 1192 Salmon, C.H., de Haan, M., Friston, K.J., Gadian, D.G., Vargha-Khadem, F., 2003. Investigat-
1193 ing individual differences in brain abnormalities in autism. *Philos. Trans. R. Soc. Lond.
1194 Ser. B Biol. Sci.* 358 (1430), 405–413.
- 1195 Sang, H., Huang, J.Z., 2012. A full scale approximation of covariance functions for large
1196 spatial data sets. *J. R. Stat. Soc. Ser. B (Stat Methodol.)* 74 (1), 111–132.
- 1197 Scarpazza, C., Sartori, G., De Simone, M.S., Mechelli, A., 2013. When the single matters
1198 more than the group: very high false positive rates in single case Voxel Based Mor-
1199 phometry. *NeuroImage* 70, 175–188.
- 1200 Seghier, M.L., Ramlackhansingh, A., Crinion, J., Leff, A.P., Price, C.J., 2008. Lesion identifica-
1201 tion using unified segmentation-normalisation models and fuzzy clustering.
1202 *NeuroImage* 41 (4), 1253–1266.
- Sehm, B., Frisch, S., Thöne-Otto, A., Horstmann, A., Villringer, A., Obrig, H., 2011. Focal
1203 retrograde amnesia: Voxel-based morphometry findings in a case without MRI
1204 lesions. *PLoS One* 6 (10), e26538.
- 1205 Teipel, S.J., Grothe, M., Lista, S., Toschi, N., Garaci, F.G., Hampel, H., 2013. Relevance of mag-
1206 netic resonance imaging for early detection and diagnosis of Alzheimer disease. *Med.
1207 Clin. North Am.* 97 (3), 399–424.
- 1208 Tohka, J., Zijdenbos, A., Evans, A., 2004. Fast and robust parameter estimation for statisti-
1209 cal partial volume models in brain MRI. *NeuroImage* 23 (1), 84–97.
- 1210 Viviani, R., Beschoner, P., Ehrhard, K., Schmitz, B., Thöne, J., 2007. Non-normality and
1211 transformations of random fields, with an application to voxel-based morphometry.
1212 *NeuroImage* 35 (1), 121–130.
- 1213 Wahba, G., 1990. Spline models for observational data. CBMS-NSF Regional Conference
1214 Series in Applied Mathematics, vol. 59. Capital City Press, Philadelphia.
- 1215 Walhovd, K.B., Westlye, L., Amlie, I., Espeseth, T., Reinvang, I., Raz, N., Agartz, I., Salat, D.,
1216 Greve, D., Fischl, B., Dale, A.M., Fjell, A.M., 2011. Consistent neuroanatomical age-
1217 related volume differences across multiple samples. *Neurobiol. Aging* 32, 916–932.
- 1218 Wang, S., Liu, P., Turkbey, B., Choyke, P., Pinto, P., Summers, R.M., 2012. Gaussian process
1219 inference for estimating pharmacokinetic parameters of dynamic contrast-enhanced
1220 MR images. *Med. Image Comput. Comput. Assist. Interv.* 15 (Pt 3), 582–589.
- 1221 Wassermann, D., Bloy, L., Kanterakis, E., Verma, R., Deriche, R., 2010. Unsupervised white
1222 matter fiber clustering and tract probability map generation: applications of a Gauss-
1223 ian process framework for white matter fibers. *NeuroImage* 51 (1), 228–241.
- 1224 Westman, E., Simmons, A., Zhang, Y., Muehlboeck, J.-S., Tunnard, C., Liu, Y., Collins, L.,
1225 Evans, A., Mecocci, P., Vellas, B., Tsolaki, M., Kloszewska, I., Soininen, H., Lovestone,
1226 S., Spenger, C., Wahlund, L.-O., AddNeuroMed consortium, 2011. Multivariate analysis
1227 of MRI data for Alzheimer's disease, mild cognitive impairment and healthy controls.
1228 *NeuroImage* 54 (2), 1178–1187.
- 1229 Westman, E., Muehlboeck, J.-S., Simmons, A., 2012. Combining MRI and CSF measures for
1230 classification of Alzheimer's disease and prediction of mild cognitive impairment
1231 conversion. *NeuroImage* 62 (1), 229–238.
- 1232 Woermann, F.G., Free, S.L., Koepp, M.J., Ashburner, J., Duncan, J.S., 1999. Voxel-by-voxel
1233 comparison of automatically segmented cerebral gray matter—a rater-independent
1234 comparison of structural MRI in patients with epilepsy. *NeuroImage* 10 (4), 373–384.
- 1235 Young, J., Modat, M., Cardoso, M.J., Mendelson, A., Cash, D., Ourselin, S., 2013. Accurate
1236 multimodal probabilistic prediction of conversion to Alzheimer's disease in patients
1237 with mild cognitive impairment. *NeuroImage Clin.* 2, 735–745.
- 1238 Zhu, F., Carpenter, T., Rodriguez Gonzalez, D., Atkinson, M., Wardlaw, J., 2012. Computed
1239 tomography perfusion imaging denoising using Gaussian process regression. *Phys.
1240 Med. Biol.* 57 (12), N183–N198.
- 1241 Ziegler, G., Dahnke, R., Gaser, C., the Alzheimer Disease Neuroimaging Initiative, 2012a.
1242 Models of the aging brain structure and individual decline. *Front. Neuroinform.* 6, 3.
- 1243 Ziegler, G., Dahnke, R., Jancke, L., Yotter, R.A., May, A., Gaser, C., 2012b. Brain structural tra-
1244 jectories over the adult lifespan. *Hum. Brain Mapp.* 33, 2377–2389.
- 1245 Ziegler, G., Dahnke, R., Winkler, A.D., Gaser, C., 2013. Partial least squares correlation of
1246 multivariate cognitive abilities and local brain structure in children and adolescents.
1247 *NeuroImage* 82, 284–294.